

# Attitude Estimation with Albedo Interference on Sun Sensor Measurements

Demet Cilden-Guler\*

*Istanbul Technical University, Istanbul, 34469, Turkey*

Hanspeter Schaub†

*University of Colorado Boulder, Colorado, 80303-0429, USA*

Chingiz Hajiyev,‡ and Zerefsan Kaymaz§

*Istanbul Technical University, Istanbul, 34469, Turkey*

**A three-axis attitude estimation scheme is presented using a set of Earth's albedo interfered coarse sun sensors (CSSs), which are inexpensive, small in size, and light in power consumption. For modeling the interference, a two-stage albedo estimation algorithm based on auto regressive (AR) model is proposed. The algorithm does not require any data such as albedo coefficients, spacecraft position, sky condition or ground coverage, other than albedo measurements. The results are compared with five albedo models on the basis of two reference conditions. The estimated albedo is fed to the CSS measurements for correction. The corrected CSS measurements are processed under three estimation techniques with two different sensor configurations. The relative performance of the attitude estimation schemes when using different albedo models is examined.**

## Nomenclature

**A** = area,  $m^2$

**a<sub>j</sub>** = the inverse variance of the sensor *j*

**B** = magnetic field,  $nT$

---

\* PhD Candidate, Aeronautics and Astronautics Engineering Department, Istanbul Technical University, Turkey; Visiting Scholar, Aerospace Engineering Sciences Department, University of Colorado Boulder, USA, and Student Member AIAA.

† Professor and Glenn L. Murphy Endowed Chair, Aerospace Engineering Sciences Department, and Fellow AIAA.

‡ Professor, Aeronautical Engineering Department.

§ Professor, Meteorological Engineering Department.

$[BR]$	=	direction cosine matrix from reference coordinates to body coordinates
$[BN]$	=	direction cosine matrix from inertial coordinates to body coordinates
$\mathbf{b}$	=	sensor observation vector in the body coordinates
$dA, \Delta A$	=	incremental area, $m^2$
$F$	=	solar flux, $W/m^2$
$f(\cdot)$	=	system function
$\mathbf{H}$	=	measurement matrix
$h(\cdot)$	=	measurement function
$I$	=	output current, $A$
$\mathbf{K}$	=	Kalman gain matrix
$N_A$	=	number of differential areas
$\hat{\mathbf{n}}$	=	unit normal vector
$p$	=	number of previous measurements
$\mathbf{r}$	=	measurement model vector in the reference coordinates
$\mathbf{r}_{sc}$	=	spacecraft position vector from an incremental area, $m$
$\hat{\mathbf{r}}_{sc}$	=	spacecraft direction vector from an incremental area
$\hat{\mathbf{s}}$	=	sun heading vector
$\mathbf{U}$	=	zero-mean Gaussian noise vector with covariance $\tilde{\mathbf{Q}}$
$V$	=	output voltage, $V$
$\mathbf{V}$	=	zero-mean Gaussian noise vector with covariance $\tilde{\mathbf{R}}$
$\mathbf{w}$	=	zero-mean Gaussian noise vector with covariance $\mathbf{Q}$
$\mathbf{x}_0$	=	initial state with mean $\boldsymbol{\mu}_0$ and covariance $\mathbf{P}_0$
$\mathbf{x}_k, \mathbf{X}_k$	=	state vector at time $t_k$
$\mathbf{y}, \mathbf{Z}$	=	measurement vector
$\hat{\mathbf{y}}$	=	prediction vector

$z_k$	=	albedo measurement at time $t_k$
$\alpha$	=	albedo coefficient
$\epsilon$	=	zero-mean Gaussian noise vector with covariance $\mathbf{R}$
$\varphi_i$	=	$i^{th}$ model parameter
$\omega$	=	angular velocity, $rad/s$
$\sigma_{B/R}$	=	modified Rodrigues parameters in body coordinates with respect to reference
$\Xi$	=	scaling term

#### *Subscripts*

A	=	central point of $dA$ on a planet
$d$	=	caused by the sun
I	=	instrument
in	=	incoming
max	=	maximum
out	=	outgoing
P	=	planet
s	=	sunlit
sc	=	spacecraft
$\alpha$	=	caused by albedo

## I. Introduction

SPACECRAFT instruments need to be oriented to achieve mission directives in space. Depending on the mission, there may be strict performance requirements in terms of attitude estimation or necessity to a safe-mode operation or sanity checks. For these purposes, additional attitude sensors such as magnetometers and sun sensors can be utilized with less accuracy but less power need, lower cost, and smaller size. Sun sensors are frequently used in both planet-orbiting satellites and interplanetary spacecraft missions in the solar system. They can be divided into two classes as fine or digital sun sensors (DSSs), and coarse sun sensors (CSSs), which are commonly used in a form of photodiodes

[1]. CSSs function almost proportional to the cosine angle between the sensor's boresight and the sun direction vector from the spacecraft. They are often used on platforms including multiple CSSs.

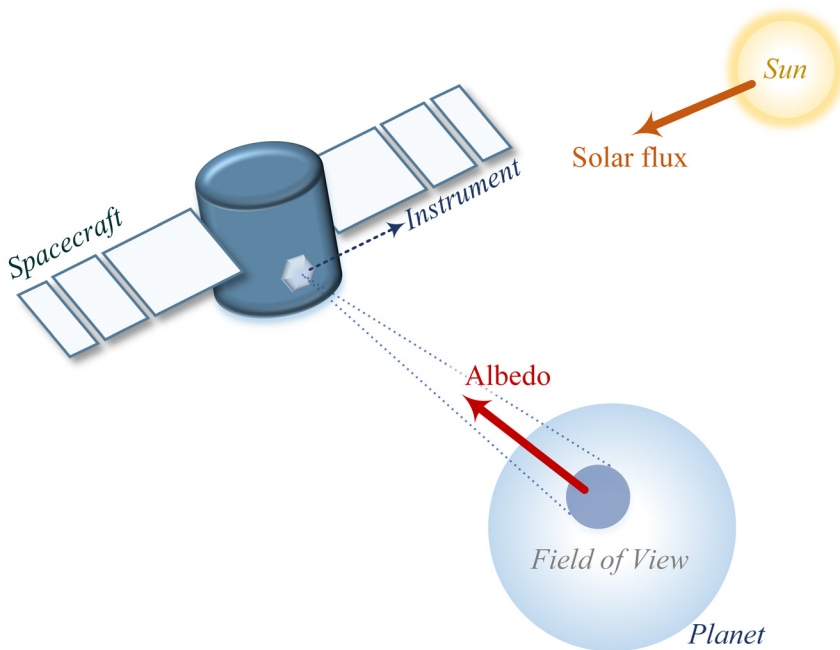


**Fig. 1 Illustration of considered radiation sources on a spacecraft.**

A spacecraft close enough to the sun and a planet receives electromagnetic radiation of direct solar flux, reflected radiation namely albedo, and emitted radiation of that planet. The solar flux is the largest source of radiation for the spacecraft while the albedo is the fraction of sunlight incident and reflected light from the planet. Spacecraft can be exposed to albedo when it sees the sunlit part of the planet (Fig. 1). The albedo values vary depending on the seasonal, geographical, diurnal changes as well as the cloud coverage. The most reflectance is caused by thickest, highest clouds while the least by snowing clouds [2]. The CSS not only measures the light from the sun but also the albedo of the planet [3]. So, a planet's albedo interference can cause anomalous sun sensor readings. According to Reference [4], albedo might worsen the sun pointing accuracy more than 20 degrees. On the other hand, albedo might be an important factor in selecting the characteristics of optical-sensor systems such as cameras or star trackers, and in spacecraft thermal and power design. For example, Reference [5] underlines that the thermal control system on the spacecraft must consider the light reflectance and emittance of the planets as it causes a highly dynamic variation in thermal load. Another study on a spacecraft thermal analysis is carried out in order to evaluate the thermal conditions for temperature

stability of sensitive instrument and radiators by using the albedo data from NASA's Clouds and Earth Radiant Energy System (CERES) instruments [6].

The mathematical model of the sun sensors can include diffusive and specular reflections from the planet which represents the perturbed sun sensor measurements. In Reference [7], perturbed sun sensor measurements are validated by the telemetry data of Ørsted satellite. The currents of the modeled CSSs are improved about three times more than the case not including any albedo model on the measurements in Reference [7], and four times in Reference [8]. A sun heading estimation algorithm is also applied by Reference [9] using extended Kalman filter (EKF). The sun direction is estimated with an accuracy under 4-degrees based on albedo interfered CSS and rate gyro (RG) measurements, and 10 degrees without RGs despite the fact that an underdetermined sun sensor coverage is considered in the study [9].

References [10] and [11] present extended consider Kalman filter (ECKF) based on modified Rodrigues parameters (MRPs) for CSS calibration. The presented filters require inertial attitude measurements but it gives scale factor accuracy less than 1% and misalignment accuracy about 1-degree even under poor attitude knowledge. Another calibration filter is proposed for photodiodes through the estimation of attitude and calibration parameters simultaneously [12]. An arbitrary number of photodiodes along with an albedo model, are calibrated using both an EKF and an unscented filter (UF). The filter estimates improve the sun vector measurements by 10-degrees and attitude by 1-degree, by combining three-axis magnetometer (TAM) and RG in the study. In order to make the albedo model lighter in computations, two constant albedo coefficients are applied rather than various spatial data in Reference [13]. From the analyses, the errors are reduced by taking the average albedo coefficient as 0.105 instead of 0.30. Even though the presented model provides a significantly better CSS accuracy for most of the times than uncorrected outputs, its predictions based on 0.30 value may occasionally overcorrect the CSS. This overcorrection causes an increase on the sensor error. It is stated that the detailed mathematical model including the albedo coefficient changes depending on the active surface elements can be used for the most accurate case but it is computationally expensive for online usage. Reference [13] concludes that because of the albedo model complexity, it is more reasonable to use a filter on the sun sensor that restricts the sensor not sensitive to the albedo. This suggestion might be more suitable for DSSs. In Reference [14], a less complex albedo model is generated via polynomial functions with 13 parameters for each albedo component including functions based on latitude and longitude. The polynomial is fitted to the reflectivity dataset from Earth Probe Total Ozone Mapping Spectrometer (TOMS) instead of using

excessive data in look-up tables. The work also estimates the spacecraft attitude states with 1-degree accuracy in nominal mode and 2-degrees in worst mode by EKF with 0.5% noisy measurements from TAM and corrected CSS.

The main purpose of our study is to estimate the albedo by using a simple model with less parameter dependency than any albedo models and to estimate the attitude by comprising the corrected CSS measurements. The estimation process using only the CSS platform and using it along with TAM is presented to be considered during the sanity checks and/or in the safe-mode operations of a spacecraft missions or in the validation algorithm of other sensors' outputs. This aids the mission by making the albedo estimates available for the other subsystems.

As a simple model, Auto Regressive (AR) albedo model is proposed. Here, the purpose is to estimate the albedo without using any data related to albedo coefficients that depend on position, time, ground and cloud coverage parameters. AR model or enhanced versions of the AR model are widely used in forecasting geomagnetic storm indices and estimating gyro drifts as well as wind speed [15–18] but to the best of our knowledge, it is used in albedo estimation for the first time in this study. The CSS measurement equations contain disturbances, most notably due to Earth's albedo, which is dependent on too many parameters. Therefore, modeling albedo is complex and computationally heavy for online usage. In the meanwhile, the AR is a simple model based on only a couple of parameters in accordance with how many measurements used. However, spacecraft's attitude information is necessary to estimate the albedo based on AR model. So, an attitude estimation procedure is also presented using the estimated albedo. Reference [7] indicates that it is possible to perform a three-axis attitude estimation by using only CSSs with albedo interference but the output equations' non-differentiability makes the estimation harder. This is why the attitude estimation procedure proposed in this study is composed by estimating the albedo first and correcting the CSS after. In this way, any albedo model is not considered in the last output equations in the attitude estimation filter.

The remainder of the paper is organized as follows. Section 2 presents the albedo and CSS mathematical models. The attitude estimation filter and AR model-based two-stage albedo estimation filter used in this study are given in Sections 3 and 4 respectively. In Section 5, the analysis and results of several scenarios for Earth's albedo data, albedo effects on CSSs, possible albedo models, and attitude estimation filters are presented and discussed. The last section summarizes and concludes the paper.

## II. Albedo and Coarse Sun Sensor Modeling

### A. Mathematical Model for a Planet's Albedo

The mathematical model for the total albedo from a planet affecting an instrument (e.g. CSS) on a spacecraft is given in this section. The parameters affecting the albedo model can be itemized as the attitude and position of the spacecraft, instrument's field of view (FOV), placement of other instruments (that might block/shadow), and albedo coefficients related to the several parameters such as ground coverage, seasonal changes, and cloudiness.

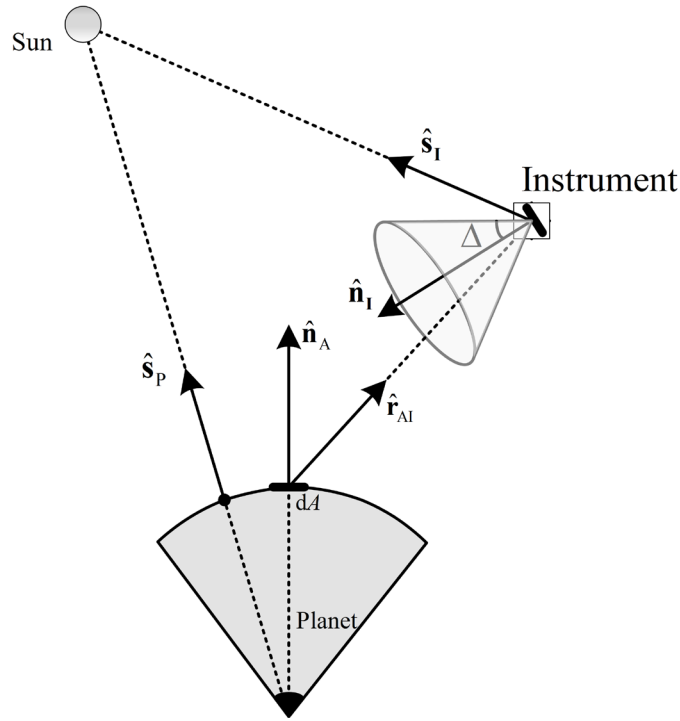


**Fig. 2 Illustration of the unit normal, sun and spacecraft heading vectors.**

The generic vectors can be described as unit normal vector ( $\hat{\mathbf{n}}$ ), sun heading vector ( $\hat{\mathbf{s}}$ ), and direction vector from A to B ( $\hat{\mathbf{r}}_{AB}$ ). In Fig. 2,  $\hat{\mathbf{n}}_A$  and  $\hat{\mathbf{n}}_I$  are the unit normal vectors of the differential area ( $dA$ ) on the planet and the instrument cell respectively,  $\hat{\mathbf{s}}_p$  and  $\hat{\mathbf{s}}_I$  are the sun heading vectors of the planet and of the instrument cell respectively.

Here, the instrument's position vector from the incremental area is  $\mathbf{r}_{AI}$  and the unit direction vector is  $\hat{\mathbf{r}}_{AI} = \frac{\mathbf{r}_{AI}}{\|\mathbf{r}_{AI}\|}$ . The spacecraft's direction vector from  $dA$  can be expressed as  $\hat{\mathbf{r}}_{sc}$ .

The differential areas,

- on the sunlit portion of the planet where  $(\hat{\mathbf{s}}_p \cdot \hat{\mathbf{n}}_A > 0)$  forming  $A_s$  (sunlit region),

- in the instrument's field of view with a half angle of  $\Delta$  where  $(-\hat{\mathbf{r}}_{AI} \cdot \hat{\mathbf{n}}_I \geq \cos(\Delta))$  forming  $A_I$  (instrument FOV region),
- in the instrument cell's maximum field of view where  $(\hat{\mathbf{r}}_{AI} \cdot \hat{\mathbf{n}}_A > 0)$  forming  $A_{I_{max}}$  (maximum area that can be seen from the instrument cell),
- in the spacecraft's field of view where  $(\hat{\mathbf{r}}_{sc} \cdot \hat{\mathbf{n}}_A > 0)$  forming  $A_{sc}$  (spacecraft FOV region),

can be used for the total albedo calculations contributing to the instrument or the spacecraft. The total area that is sunlit and visible to the instrument results in  $A \equiv A_s \cap A_I$  (see Fig. 3).

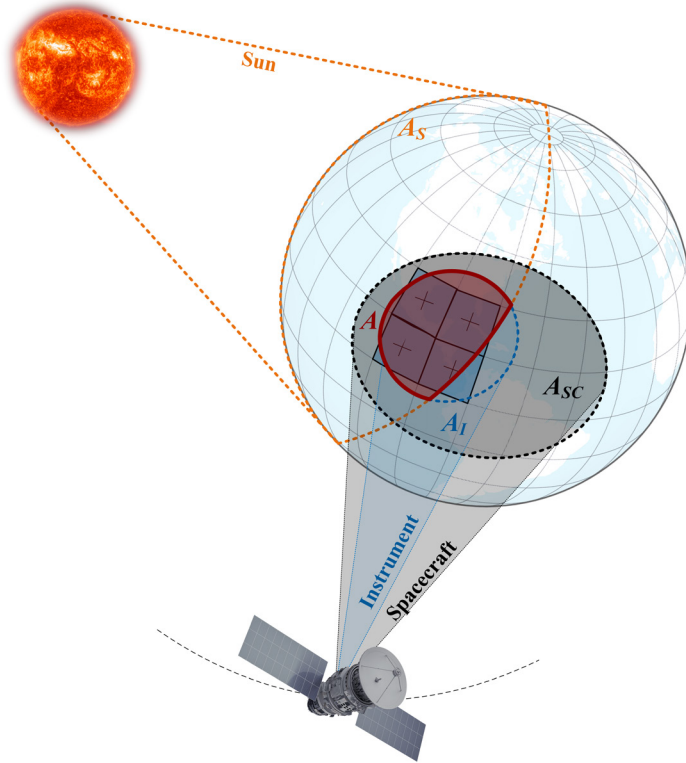


**Fig. 3 Illustration of the observed illuminated area.**

The solar flux reaching to a point is found as  $F_{\text{sun}} (\hat{\mathbf{s}} \cdot \hat{\mathbf{n}})$  in  $W/m^2$  when using the generic vectors. So, the solar flux reaching the incremental area ( $F_{in}$ ) is [3],

$$F_{in} = F_{\text{sun}} (\hat{\mathbf{s}}_p \cdot \hat{\mathbf{n}}_A), \quad (1)$$

where  $F_{\text{sun}}$  is the solar constant at the top of the atmosphere. The mean value of the solar flux at the mean distance of the sun-planet is called solar constant which slightly changes depending on the solar cycle and the planet's distance from the sun. The solar constant value for Earth is  $1366.1 \text{ W/m}^2$ . The incoming solar flux is both absorbed and reflected partially. The reflected portion is proportional to the albedo coefficient ( $\alpha$ ) as,

$$\begin{aligned} F_{\text{out}} &= \alpha F_{\text{in}} \\ &= \alpha F_{\text{sun}} (\hat{s}_p \cdot \hat{n}_A). \end{aligned} \quad (2)$$

Using the conservation of energy [3], the irradiance due to the planet's albedo at the spacecraft's position is,

$$F_\alpha = \frac{F_{\text{sun}}}{\pi} \iint_A \frac{\alpha (\hat{s}_p \cdot \hat{n}_A) (\hat{r}_{AI} \cdot \hat{n}_A) (-\hat{r}_{AI} \cdot \hat{n}_I)}{\|\hat{r}_{AI}\|^2} dA, \quad (3)$$

where  $F_{\text{sun}}$  is the solar constant at the top of the atmosphere,  $\hat{s}_p$  is the sun heading vector of the planet,  $\hat{n}_A$  and  $\hat{n}_I$  are the unit normal vectors of  $dA$  and the instrument cell respectively,  $\hat{r}_{AI}$  is the unit direction vector to the instrument from  $dA$ . Eq. (3) is rewritten in a summation form in order to obtain a discrete version as [19],

$$F_\alpha = \frac{F_{\text{sun}}}{\pi} \sum_{i=1}^{N_A} \frac{\alpha (\hat{s}_p \cdot \hat{n}_{A_i}) (\hat{r}_{AI_i} \cdot \hat{n}_{A_i}) (-\hat{r}_{AI_i} \cdot \hat{n}_I)}{\|\hat{r}_{AI_i}\|^2} \Delta A, \quad (4)$$

where  $N_A$  is the number of differential areas ( $\Delta A$ ) inside the intersectional area,  $A$ .

## B. Albedo Coefficients

Albedo coefficient ( $\alpha$ ) is the ratio of the reflected and incoming solar radiation over a unit area that ranges from zero to one. As it is described in the previous section, the data is required to comprise albedo based on latitude and longitude of a planet and it might optionally include information of date/time, cloudiness, etc. The most reflective planet in the solar system is Venus by its global Bond albedo around 0.76 [20]. The Earth's average albedo evolved over time but converged to 0.29 in the mean in the last 40 years, and had only 0.2% interannual variability on global mean albedo [21]. In order not to model a complex albedo close to the real case which depends on many parameters

as discussed, a constant global albedo coefficient can be used. However, the use of this kind of straightforward planet interference might be insufficiently accurate [13].

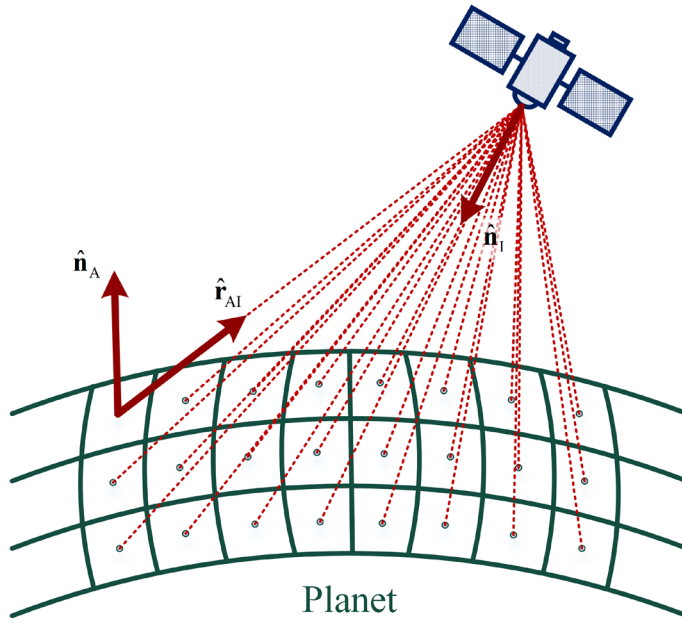


**Fig. 4 Illustration of the albedo influence on an instrument from observed incremental areas of a planet.**

In order to determine the total albedo affecting the instrument, the planet should be divided into grids based on the albedo data size. Fig. 4 shows an illustration of the albedo contributions from each grid element within the field of view to the instrument. The albedo data might include irregularities on the latitude and longitude (see Fig. 5). The grid elements to be considered can be determined using their central points. The grid element with the central point within the field of view can be considered as an active element. In Fig. 5, regular and irregular grid examples are given. Even the area seen is the same (red elliptical area), the active grid elements to be used (blue rectangular areas) for the calculations differentiate. Another method to apply here is to utilize an interpolation technique [22] such as inverse distance weighting, kriging, bi-cubic, nearest-neighbor, etc. so as to use the exact area of interest in the calculations. It is also possible to convert the irregular grids into the regular version.

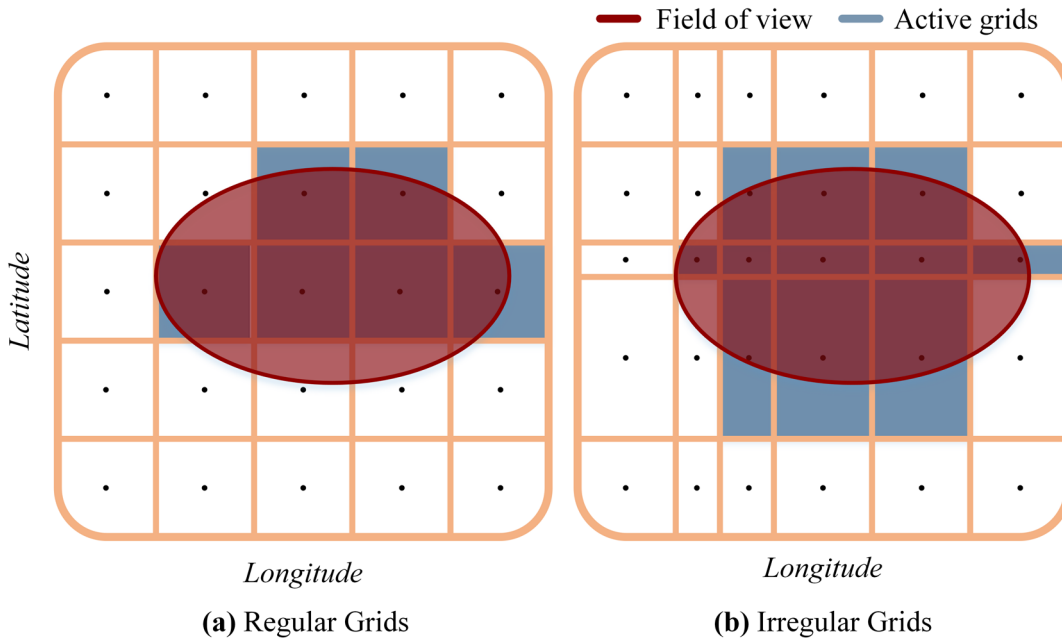


**Fig. 5 Illuminated field of view area with regular (a) and irregular (b) grid examples.**

The albedo data of Mars can be obtained from the instrument Thermal Emission Spectrometer (TES)<sup>\*</sup> on the Mars Global Surveyor (MGS) spacecraft launched in 1996. The data has irregularities in the sense of latitude and longitude intervals.

The Earth's albedo data can be obtained from the instruments such as TOMS<sup>†</sup> and CERES<sup>‡</sup>. The TOMS measures the albedo of the Earth's atmosphere in the near-ultraviolet region. The data are mapped with a grid size of 180 x 288 and a latitude and longitude resolution of  $1^\circ \times 1.25^\circ$ . The most recent data are obtained from the Earth Probe mission between 1996 and 2006. The CERES shares the albedo data up to with  $1^\circ \times 1^\circ$  resolution with surface albedo or Top of the Atmosphere (TOA) albedo options under clear-sky and all-sky conditions. The clear-sky monthly mean TOA fluxes from CERES are provided completely cloud-free according to Moderate Resolution Imaging Spectroradiometer (MODIS) data with 1-km resolution [23, 24]. There are several satellites having CERES instrument onboard such as TRMM, Terra, Aqua, Suomi NPP, and NOAA-20. Terra and Aqua satellites have two CERES instrument pair to

\* <http://tes.asu.edu/>

† <https://ozoneeq.gsfc.nasa.gov/>

‡ <https://ceres.larc.nasa.gov/>

provide an enhanced product quality. The hourly, daily and monthly satellite pair (Terra-Aqua) data are available starting from 2002. A sample Earth's albedo coefficient data from CERES averaged over 2018 is presented in Fig. 6.

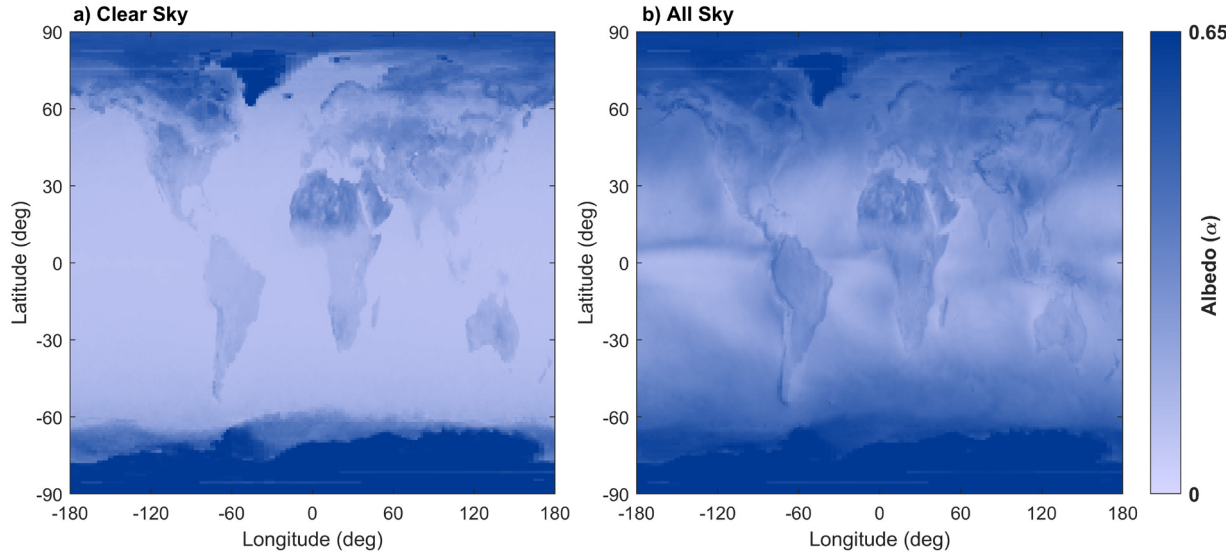


**Fig. 6 Albedo coefficients averaged over CERES 2018 monthly data under clear-sky (a) and all-sky (b) conditions.**

### C. Modeling of Coarse Sun Sensor Measurements in the presence of Albedo

As the CSS senses any light received, the light reflected from a celestial body will also affect the sensor. Here, one celestial body is considered close enough to a spacecraft for modeling the CSS measurements without having any blockage to the sensor's FOV from the structural components of the spacecraft. Adding more than one celestial body to the simulations is possible by adding another albedo summing term. The structural blockage can be avoided at the design stage or modeled in the FOV of the CSS. The process of simulating the CSS readings excited by the planet's albedo is given in Fig. 7.

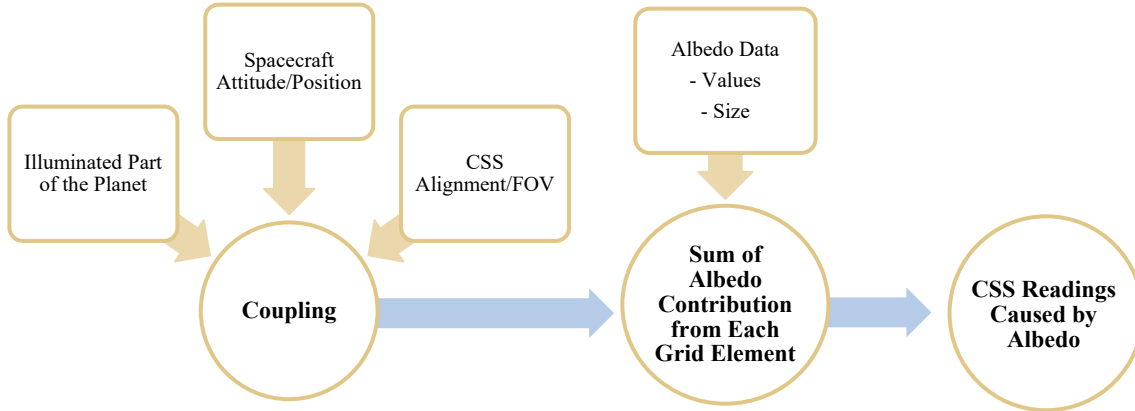


**Fig. 7** The process for simulating the CSS albedo readings.

The output current of CSS is proportional to the angle between the sensor's boresight and the direction of the light source in general [3]. By using the solar irradiance formula on an instrument as  $F_{\text{sun}}(\hat{s}_I \cdot \hat{n}_I)$ , the output current generated from CSS can be expressed as,

$$I_d = \begin{cases} I_{\max} \frac{F_{\text{sun}}}{F_{\text{cal}}} (\hat{s}_I \cdot \hat{n}_I) & \text{if } (\hat{s}_I \cdot \hat{n}_I > 0) \cap (\hat{s}_I \cdot \hat{n}_I \geq \cos(\Delta)) \\ 0 & \text{otherwise} \end{cases} \quad (5)$$

where  $F_{\text{cal}}$  is the calibration flux determined during ground testing,  $I_{\max}$  is the possible maximum output current of CSS. The current of CSS contributed from albedo is written as [7],

$$I_\alpha = \begin{cases} I_{\max} \frac{F_{\text{sun}}}{F_{\text{cal}}} \sum_{i=1}^{N_A} \frac{\alpha (\hat{s}_I \cdot \hat{n}_{A_i}) (\hat{r}_{A_i} \cdot \hat{n}_{A_i}) (-\hat{r}_{A_i} \cdot \hat{n}_I)}{\pi \|\hat{r}_{A_i}\|^2} \Delta A, & \text{if } \Delta A \in A \\ 0 & \text{if } \Delta A \notin A \end{cases} \quad (6)$$

The resulting CSS current gives,

$$I = I_d + I_\alpha + \varepsilon_{\text{CSS}}, \quad (7)$$

where  $\varepsilon_{\text{CSS}}$  is zero-mean Gaussian noise on the measurements. One might need to use voltage outputs depending on the given instrumental datasheet. The voltage output can be calculated in a similar manner by including the maximum voltage of CSS,  $V_{\max}$  instead of  $I_{\max}$  in calculating  $V_d$  and  $V_\alpha$ . The resulting voltage of CSS is,

$$V = V_d + V_\alpha + \varepsilon_{\text{CSS}}. \quad (8)$$

The presented CSS readings in a current or a voltage format belong to only one photodiode and the calculations need to be repeated for as many photodiodes as are available.

### III. Gaussian Estimation Filters

The general estimation state-space problem is expressed as,

$$\mathbf{x}_k = f(\mathbf{x}_{k-1}) + \mathbf{w}_k, \quad (9)$$

$$\mathbf{y}_k = h_k(\mathbf{x}_k) + \mathbf{\varepsilon}_k, \quad (10)$$

where  $f(\cdot)$  is the system and  $h(\cdot)$  is the measurement function,  $\mathbf{x}_k$  is the state vector at a time  $t_k$ ,  $\mathbf{w}_k$  is the zero-mean Gaussian noise vector with the covariance of  $\mathbf{Q}$ ,  $\mathbf{y}_k$  is the measurement vector, and  $\mathbf{\varepsilon}_k$  is the zero-mean Gaussian noise vector with the covariance of  $\mathbf{R}_k$ . The initial state is  $\mathbf{x}_0$  with mean  $\mathbf{\mu}_0$  and covariance  $\mathbf{P}_0$ ; its probability density function (PDF) can be denoted as  $p(\mathbf{x}_0) = N(\mathbf{x}_0 | \mathbf{\mu}_0, \mathbf{P}_0)$ . Approximations based on Kalman filtering can be represented using the Gaussian filter (GF) technique [25]. This technique uses the parameters  $\mathbf{\mu}_k$ ,  $\mathbf{P}_k$  in  $p(\mathbf{x}_k | \mathbf{y}_{1:k}) = N(\mathbf{x}_k | \mathbf{\mu}_k, \mathbf{P}_k)$  for the distribution of state estimation by two stages. The first stage is composed of predictions using the system function to determine the predicted mean,

$$\bar{\mathbf{\mu}}_k = \int f(\mathbf{x}_{k-1}) N(\mathbf{x}_{k-1} | \mathbf{\mu}_{k-1}, \mathbf{P}_{k-1}) d\mathbf{x}_{k-1}, \quad (11)$$

and the predicted covariance,

$$\mathbf{P}_k^- = \int (f(\mathbf{x}_{k-1}) - \boldsymbol{\mu}_{k-1})(f(\mathbf{x}_{k-1}) - \boldsymbol{\mu}_{k-1})^T N(\mathbf{x}_{k-1} | \boldsymbol{\mu}_{k-1}, \mathbf{P}_{k-1}) d\mathbf{x}_{k-1} + \mathbf{Q}. \quad (12)$$

The second stage updates the predictions using the measurements as,

$$\hat{\mathbf{y}}_k = \int \mathbf{h}_k(\mathbf{x}_k) N(\mathbf{x}_k | \boldsymbol{\mu}_k^-, \mathbf{P}_k^-) d\mathbf{x}_k, \quad (13)$$

$$\boldsymbol{\Psi}_k = \int (\mathbf{x}_k - \boldsymbol{\mu}_k^-)(\mathbf{h}_k(\mathbf{x}_k) - \hat{\mathbf{y}}_k)^T N(\mathbf{x}_k | \boldsymbol{\mu}_k^-, \mathbf{P}_k^-) d\mathbf{x}_k, \quad (14)$$

$$\boldsymbol{\Phi}_k = \int (\mathbf{h}_k(\mathbf{x}_k) - \hat{\mathbf{y}}_k)(\mathbf{h}_k(\mathbf{x}_k) - \hat{\mathbf{y}}_k)^T N(\mathbf{x}_k | \boldsymbol{\mu}_k^-, \mathbf{P}_k^-) d\mathbf{x}_k. \quad (15)$$

The innovation can be found as,

$$\mathbf{e}_k = \mathbf{y}_k - \hat{\mathbf{y}}_k, \quad (16)$$

with the innovation covariance,

$$\mathbf{S}_k = \boldsymbol{\Phi}_k + \mathbf{R}_k, \quad (17)$$

which is used in constituting the Kalman gain as,

$$\mathbf{K}_k = \boldsymbol{\Psi}_k \mathbf{S}_k^{-1}. \quad (18)$$

Finally, the posterior mean and the associated covariance can be found as:

$$\boldsymbol{\mu}_k = \boldsymbol{\mu}_k^- + \mathbf{K}_k \mathbf{e}_k, \quad (19)$$

$$\mathbf{P}_k = \mathbf{P}_k^- - \mathbf{K}_k \mathbf{S}_k \mathbf{K}_k^T, \quad (20)$$

The integrals given in Equations (11) to (15) can be approximated using different Kalman-type filters [26, 27]. The attitude of a spacecraft can be estimated using conventional approaches, namely, the EKF [28] or unscented Kalman

filter (UKF), which is derivative-free [29], based on nonlinear system and measurement functions defined in Equations (9) - (10). An EKF is used in this study and the attitude is represented using modified Rodrigues parameters (MRPs) indicated with  $\sigma_{B/R}$  symbol, which is in body coordinates with respect to the reference (inertial) coordinates [30, 31].

Another approach is using a deterministic attitude determination techniques called single-frame methods (SFMs) as a sub-step in order to make the attitude part of the measurements linear with respect to the states [32–36]. The SFM based preprocessing step is also implemented before the update stage of the filter by minimizing Wahba's loss function [37],

$$L(\mathbf{A}_k) = \frac{1}{2} \sum_j \mathbf{a}_{j_k} \left| \mathbf{b}_{j_k} - [\mathbf{BR}]_k \mathbf{r}_{j_k} \right|^2, \quad (21)$$

where  $[\mathbf{BR}]$  is the direction cosine matrix from reference coordinates to body coordinates,  $\mathbf{a}_j$  is the inverse variance of the sensor  $j$ ,  $\mathbf{b}_j$  is the sensor observation vector in the body coordinates, and  $\mathbf{r}_j$  is the measurement model vector in the reference coordinates. The attitude can be determined by SFM and used in the Gaussian filters as linear attitude measurements. The loss function can be minimized using one of the SFM methods namely SVD, QUEST, q, FOAM etc. [33, 38].

The attitude measurements from SFM is,

$$\tilde{\mathbf{y}}_k = \mathbf{Hx}_k + \boldsymbol{\varepsilon}_k, \quad (22)$$

where the part of the measurement matrix corresponding to the attitude states is an identity matrix,  $\tilde{\mathbf{y}}_k$  is the attitude measurements with covariance  $\tilde{\mathbf{R}}_k$  which is updated inherently by SFM. The innovation in Eq. (16) is replaced by,

$$\mathbf{e}_k = \tilde{\mathbf{y}}_k - \hat{\mathbf{y}}_k \quad (23)$$

and Eq. (17) by,

$$\mathbf{S}_k = \mathbf{H}\mathbf{P}_k^{-1}\mathbf{H}^T + \tilde{\mathbf{R}}_k. \quad (24)$$

SFM-aided Kalman filters are expected to benefit from having the initial attitude determined by SFM, especially for the transient region of the estimations. According to Reference [33], the singular value decomposition (SVD) method is faster than the q method and more robust than the computationally fast methods e.g. FOAM and ESOQ [39]. In this regard, SVD, SVD-aided EKF, and conventional EKF estimation methods are implemented to the computer simulations in this work.

#### A. Measurement Models of the Attitude Sensors

In this study, a spacecraft is considered to have two or three measurement sensors out of CSS, TAM, and RG, since these sensors are commonly used for spacecraft missions.

Each CSS can be modeled using Eq. (7), which gives the current generated by one CSS in the body frame. For the platform, the sun direction measurement vector can be obtained as,

$$\mathbf{y}_{\text{css}} = \sum_{i=1}^{N_{\text{css}}} I_i \cdot \hat{\mathbf{n}}_{\text{css}_i}, \quad (25)$$

where  $\hat{\mathbf{n}}_{\text{css}_i}$  is the unit normal vector of the  $i^{\text{th}}$  CSS cell and  $N_{\text{css}}$  is the number of CSSs.

TAM measurements can simply be modeled as,

$$\mathbf{B}_{\text{tam}} = [BN] \mathbf{B}_{\text{model}} + \boldsymbol{\varepsilon}_{\text{tam}}, \quad (26)$$

where  $[BN]$  is the direction cosine matrix from inertial to the body frame,  $\boldsymbol{\varepsilon}_{\text{tam}}$  is the zero-mean Gaussian magnetometer measurement noise vector and  $\mathbf{B}_{\text{model}}$  is the magnetic field model outputs, such as those of the International Geomagnetic Reference Field (IGRF), World Magnetic Model (WMM), dipole model, etc. [40, 41]. IGRF is used for this work.

Rate gyros are used in order to model the angular velocity of the spacecraft. The measurements can be modeled as,

$$\boldsymbol{\omega}_{RG} = \boldsymbol{\omega}_{BN} + \boldsymbol{\varepsilon}_{RG}, \quad (27)$$

where  $\omega_{RG}$  are the body measured angular rates based on the spacecraft dynamics model angular velocity  $\omega_{BN}$  of the body frame with respect to the inertial frame, and  $\varepsilon_{RG}$  is the zero-mean Gaussian gyroscope measurement noise vector.

#### IV. Two-Stage Albedo Estimation Filter using Auto Regressive Model

This section presents a two-stage estimation using AR time-series approximation for the planet's albedo estimation. The AR model is based on simple summing term, which uses a number of previous measurements, and a noise term as,

$$z_k = \sum_{i=1}^p (\varphi_i z_{k-i}) + \varepsilon_k, \quad (28)$$

where  $z_k$  represents one component of the albedo measurements (the difference between the sun sensor measurements in the body frame, and the sun direction model transformed into body frame using the spacecraft's attitude information),  $\varphi$  is the model parameters,  $p$  is the number of previous measurements to be used, and  $\varepsilon_k$  is the zero-mean Gaussian noise. Akaike criterion (AIC) can be used to determine the order of the AR model [42]. The first stage estimates the AR model parameters using the recursive least squares (RLS) method. By substituting the collected measurements of  $z_k$ , the matrix form of the measurement equation can be expressed as,

$$Y_k = \tilde{\mathbf{Z}}_k \Phi_k + \varepsilon_k, \quad (29)$$

where  $Y_k = z_k$ ,  $\tilde{\mathbf{Z}}_k = [z_{k-1} \ z_{k-2} \ \cdots \ z_1]$ ,  $\Phi_k = [\varphi_1 \ \varphi_2 \ \cdots \ \varphi_{k-1}]^T$ . The formula for the estimation of the model parameters can be written as [17],

$$\Phi_{k+1} = \Phi_k + \Xi_k (Y_k - \tilde{\mathbf{Z}}_k \Phi_k). \quad (30)$$

Here, the scaling ( $\Xi_k$ ) in the correction term is determined by,

$$\Xi_k = \frac{1}{1 + \tilde{\mathbf{Z}}_k \Gamma_k \tilde{\mathbf{Z}}_k^T} \Gamma_k \tilde{\mathbf{Z}}_k^T, \quad (31)$$

where

$$\Gamma_k = (\tilde{\mathbf{Z}}_k^T \tilde{\mathbf{Z}}_k)^{-1}. \quad (32)$$

The model parameters ( $\Phi_{k+1}$ ) estimated from Eq. (30) can be used in the second stage. The linear system is defined as [17],

$$\mathbf{X}_k = \mathbf{F}_k \mathbf{X}_{k-1} + \mathbf{B}_k \mathbf{U}_k, \quad (33)$$

and the measurement is,

$$\mathbf{Z}_k = \mathbf{H} \mathbf{X}_k + \mathbf{V}_k. \quad (34)$$

where  $\mathbf{X}_k = [z_k \ z_{k-1} \ \dots \ z_{k-p+1}]_{1 \times p}^T$  is the state vector,  $\mathbf{U}_k = [\varepsilon_k \ 0 \ \dots \ 0]_{1 \times p}^T$  is the zero-mean Gaussian noise vector with the process noise covariance matrix ( $\mathbf{Q}$ ),  $\mathbf{V}_k$  is the zero-mean Gaussian noise vector with the measurement covariance matrix ( $\mathbf{R}$ ),  $\mathbf{H} = [1 \ 0 \ \dots \ 0]_{1 \times p}$  is the measurement matrix, and  $\mathbf{F}_k$  and  $\mathbf{B}$  are given as:

$$\mathbf{F}_k = \begin{bmatrix} \varphi_1 & \varphi_2 & \dots & \varphi_p \\ 1 & 0 & \dots & 0 \\ \vdots & \vdots & \ddots & \vdots \\ 0 & 0 & 0 & 0 \end{bmatrix}_{p \times p}, \quad (35)$$

$$\mathbf{B} = \begin{bmatrix} 1 & 0 & \dots & 0 \\ 0 & 0 & \dots & 0 \\ \vdots & \vdots & \ddots & \vdots \\ 0 & 0 & \dots & 0 \end{bmatrix}_{p \times p}. \quad (36)$$

The Kalman type filtering algorithm based on the defined system and the measurement functions estimate the albedo state vector using the same procedure described in the previous section defined the Equations (16) - (20). The innovation in Eq. (16) is replaced by,

$$\mathbf{e}_k = \mathbf{Z}_k - \mathbf{H}\boldsymbol{\mu}_k^- . \quad (37)$$

The innovation covariance in Eq. (17) is replaced by,

$$\mathbf{S}_k = \mathbf{H}\mathbf{P}_k^- \mathbf{H}^T + \mathbf{R}. \quad (38)$$

Finally, the Kalman gain in Eq. (18) is replaced by,

$$\mathbf{K}_k = \mathbf{P}_k^- \mathbf{H}^T \mathbf{S}_k^{-1}, \quad (39)$$

for representing the Kalman filtering of the second stage estimation. By using the two-stage estimation form, the albedo of a planet can be estimated at each time step.

## V. Analysis and Results

### A. Earth's Albedo Data and Sun Sensor Measurements

Eleven years of Synoptic TOA and surface fluxes and clouds (SYN) 4.1 edition of Terra-Aqua satellite pair CERES data product is used with  $1^\circ \times 1^\circ$  global grid of Earth. The global albedo for 11 years from 2008 to 2018 is presented using box plots for each month in Fig. 8 under clear-sky and all-sky conditions. The small range of the box plots of each month demonstrates that the interannual albedo does not significantly change over the years for any month. While the averages slightly change or do not differ in years, values depending on the month grossly vary under both sky conditions with a similar trend. Especially the months between May and August, and the rest of the months are highly different than each other. The trend of the plots is similar for the clear-sky and all-sky cases. The lines on the figures are Fourier series model based fitted curves to the mean values from the box plots of each month identified as the red color for the all-sky condition and blue for the clear-sky. All-sky condition is almost as twice as the clear-sky albedo

averages. From the data, the global average of the albedo over the years and months is found to be about 0.23 under clear-sky and 0.37 under the all-sky condition.

The albedo coefficients given in Fig. 9 are 11-year (2008-2018) averaged over 4 consecutive seasons as Season 1 (December-January-February), Season 2 (March-April-May), Season 3 (June-July-August), and Season 4 (September-October-November). The values are distributed based on the data under clear-sky and all-sky conditions globally. The albedo differentiates globally with the seasonal changes and with the sky conditions. The coefficients for each season and sky condition are presented by the maps prepared using the Hammer–Aitoff projection [43]. The null grids are shown with the white color, which is not excessive for the monthly mean data, and the continents with the black lines. In this way, the albedo dependency on the land coverage can be realized, which is more noticeable in the clear-sky condition than the all-sky. Because the cloud cover in the all-sky case causes the neighboring regions having similar albedo and reduces the ground cover effects. In addition to the cloud formations, the highest reflectivity are observed in the polar regions and Greenland [14].

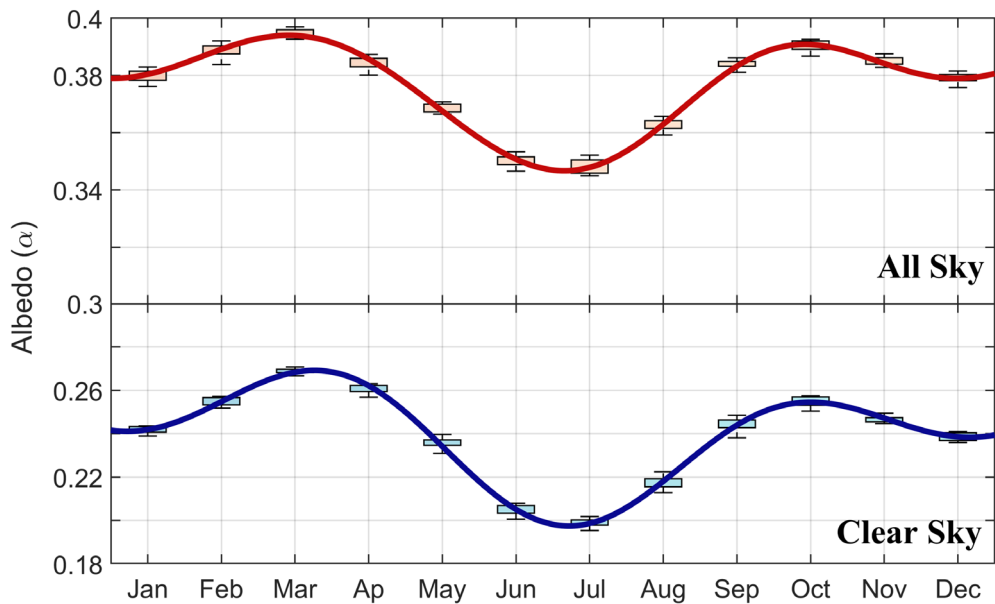
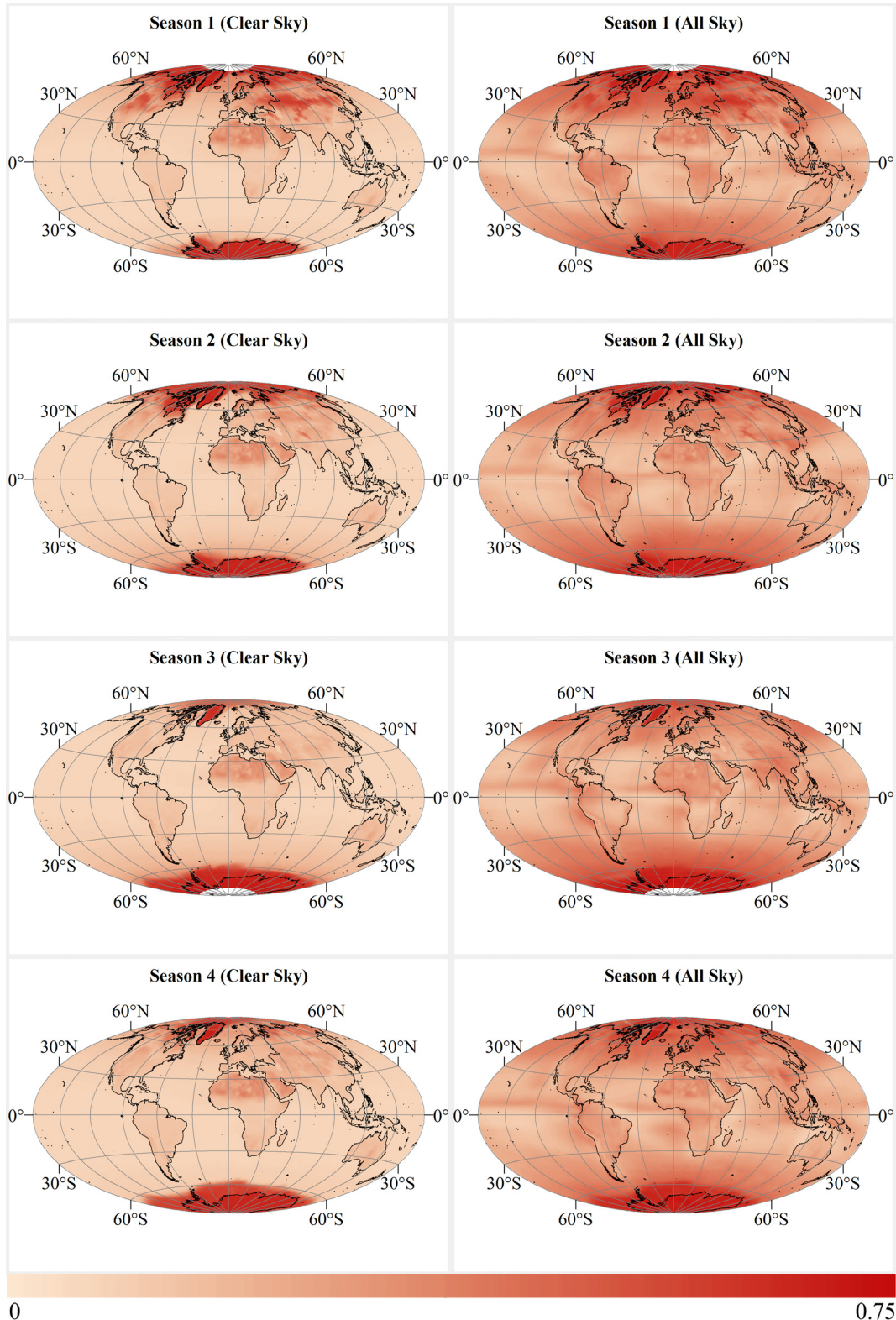


**Fig. 8 Monthly albedo box plots for 11 years under clear-sky (bottom) and all-sky (top) conditions.**

The albedo coefficients in Table 1 and Table 2 are also 11-year averaged values using spatial and seasonal scales. The spatial scales include global, tropics, polar and midlatitude regions at the north (N) and south (S) hemispheres, while the seasonal scales have four time intervals as described. The values are averaged based on clear-sky (Table 1)

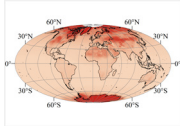
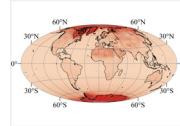
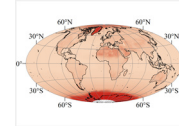
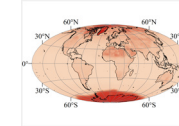
and all-sky (Table 2) conditions. The cells with no data are ignored in the averaging process. Several remarks can be itemized by looking at the albedo variations as,

- The maximum averaged albedo is at the polar regions under all cases.
- Albedo is the most effective in boreal winter (December-January-February) at the northern hemisphere and in austral winter (June-July-August) in the southern hemisphere under all cases.
- The peak values are found in the same spatial regions under the all-sky condition (minimum at the tropics and maximum at the polar south region).
- The peak values are found in slightly different spatial regions under clear-sky conditions.
- All values are greater in the all-sky case comparing to the clear-sky.
- The look-up table can be implemented for attitude estimation purposes by dividing the planet into spatial regions and seasonal periods for less computation instead of using every grid on the planet over several years.

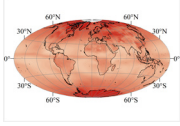
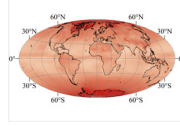
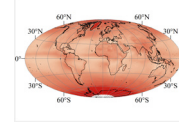
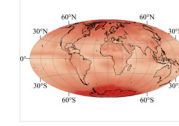


**Fig. 9** 11-year averaged global albedo coefficients over 4-seasons under clear-sky (left) and all-sky (right) conditions.

**Table 1** 11-year averaged albedo coefficients over regions and seasons indicated (Clear-sky).

<b>Averaging Scale</b>	<b>Season 1</b>	<b>Season 2</b>	<b>Season 3</b>	<b>Season 4</b>	
	<b>Dec-Jan-Feb</b>	<b>Mar-Apr-May</b>	<b>Jun-Jul-Aug</b>	<b>Sep-Oct-Nov</b>	
					
<b>Global</b>	0.3017	0.2999	0.2704	0.2852	
<b>Polar North (<math>60^{\circ}</math> – <math>90^{\circ}</math> N)</b>	<b>0.5310</b>	0.5068	0.3093	0.4224	
<b>Midlatitude North (<math>30^{\circ}</math> – <math>60^{\circ}</math> N)</b>	0.2602	0.1798	0.1370	0.1792	
<b>Tropics (<math>30^{\circ}</math> N – <math>30^{\circ}</math> S)</b>	0.1210	0.1178	0.1195	0.1177	
<b>Midlatitude South (<math>30^{\circ}</math> – <math>60^{\circ}</math> S)</b>	0.1017	0.1476	0.1779	0.1165	
<b>Polar South (<math>60^{\circ}</math> – <math>90^{\circ}</math> S)</b>	0.4947	<b>0.5475</b>	<b>0.6082</b>	<b>0.5905</b>	

**Table 2** 11-year averaged albedo coefficients over regions and seasons indicated (All-sky).

<b>Averaging Scale</b>	<b>Season 1</b>	<b>Season 2</b>	<b>Season 3</b>	<b>Season 4</b>	
	<b>Dec-Jan-Feb</b>	<b>Mar-Apr-May</b>	<b>Jun-Jul-Aug</b>	<b>Sep-Oct-Nov</b>	
					
<b>Global</b>	0.4346	0.4270	0.4110	0.4252	
<b>Polar North (<math>60^{\circ}</math> – <math>90^{\circ}</math> N)</b>	0.5910	0.5692	0.4636	0.5461	
<b>Midlatitude North (<math>30^{\circ}</math> – <math>60^{\circ}</math> N)</b>	0.4309	0.3465	0.3016	0.3536	
<b>Tropics (<math>30^{\circ}</math> N – <math>30^{\circ}</math> S)</b>	0.2350	0.2242	0.2361	0.2315	
<b>Midlatitude South (<math>30^{\circ}</math> – <math>60^{\circ}</math> S)</b>	0.3205	0.3687	0.3986	0.3414	
<b>Polar South (<math>60^{\circ}</math> – <math>90^{\circ}</math> S)</b>	<b>0.5955</b>	<b>0.6261</b>	<b>0.6550</b>	<b>0.6535</b>	

For analyzing the effects of Earth's albedo on CSS measurements, it is possible to use an arbitrary year rather than the exact year of spacecraft flight since the average values do not differ significantly in years by referring to Fig. 8. The data sample averaged over arbitrarily chosen year, 2018 is employed (Fig. 6). A scenario is performed for observing the albedo effects on the CSS measurements particularly.

Here, CSS platforms are put on every face for convenience in Earth's albedo observation. Photo-diode placements on each CSS platform is illustrated in Fig. 10 in platform coordinates  $\{\hat{p}_1, \hat{p}_2, \hat{p}_3\}$ . Each CSS has  $\Delta = 60^\circ$  half field of view angle and is assumed to read a maximum of 1 A under direct sunlight.

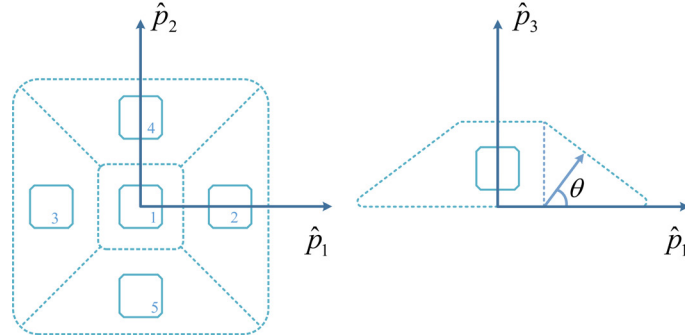


**Fig. 10 Illustration of CSS placement on each platform.**

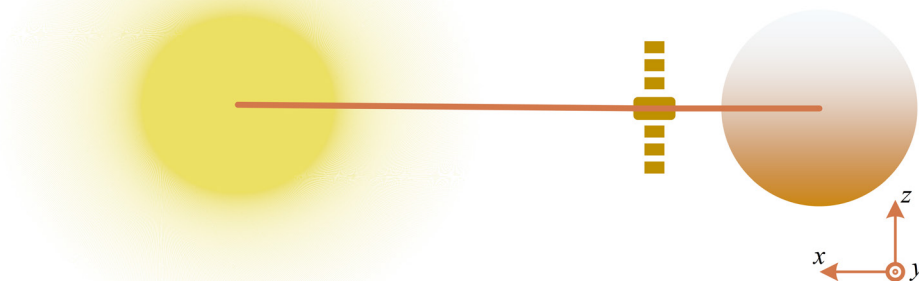


**Fig. 11 Illustration of sun, spacecraft, and Earth positions for Scenario 1.**

For the first spacecraft setup, a fixed craft with no rotational dynamics is placed on the Sun-Earth line at 800 km altitude for simplicity in observing the CSS outputs. In Fig. 11, the positions of sun, spacecraft, and Earth are illustrated without scaling. In this scenario, a symmetrical behavior might be expected in CSS platform outputs on spacecraft-face-counterparts in terms of only sun exposure except for  $+x$  and  $-x$  directions. Here,  $+x$  is pointing to sun, and  $-x$  to Earth. However, albedo also excites the CSS. The satellite faces are numbered respectively for  $+x, +y, +z, -x, -y, -z$  directions in Fig. 11. For the analysis, Face 4 ( $-x$  direction) of the satellite, which is exposed only to Earth's albedo and not to sun, is used. In order to inspect the parameter dependence of albedo, two parameters,

- Altitude
- Longitude

are tested by differentiating one parameter and fixing the others. The field of view of each CSS on Face-4, in which the outer frame is marked with a black line, can be seen in Fig. 12. The base albedo map behind each region is the left panel (a) of Fig. 6.

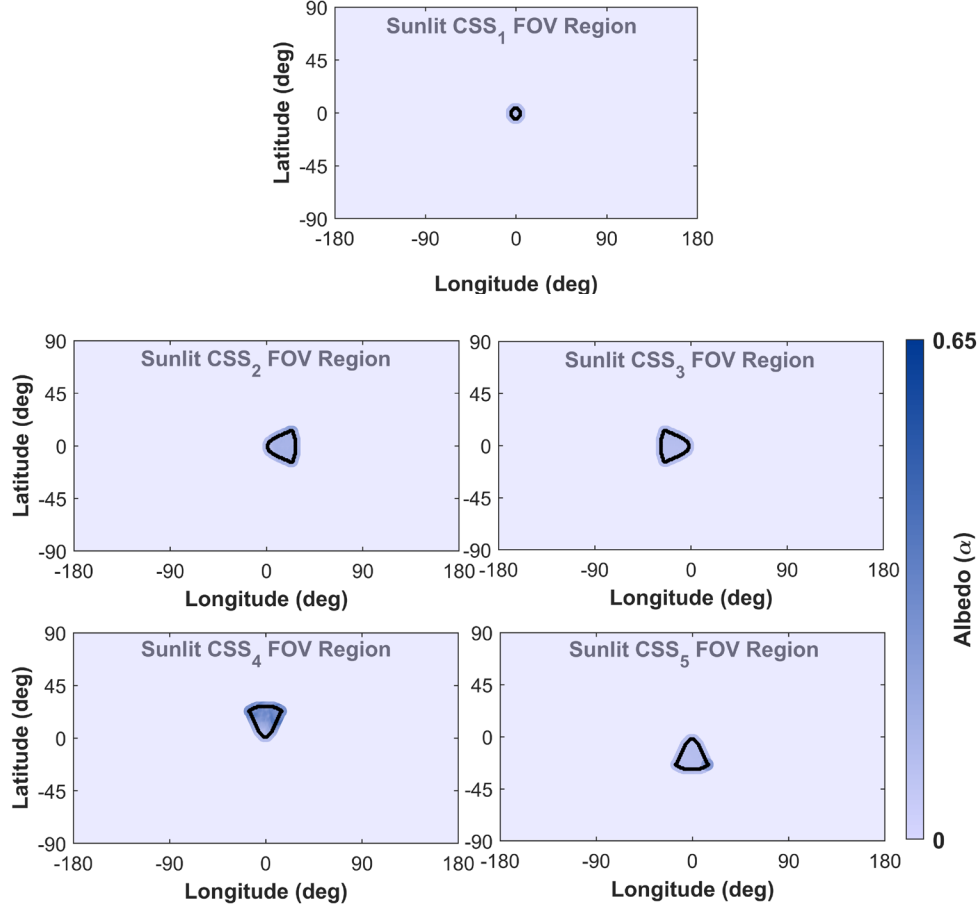


**Fig. 12 CSS field of views on Face 4 of the satellite at 800 km altitude.**

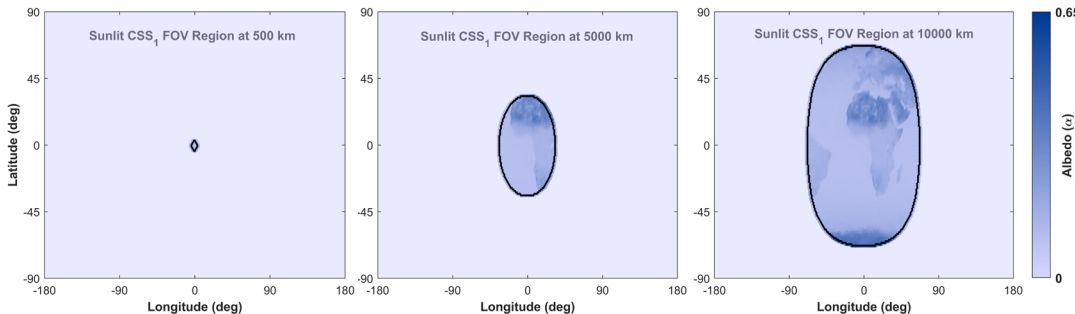


**Fig. 13 CSS-1 field of view on Face 4 of the satellite at three different altitudes (left to right: 500 km, 5000 km, and 10000 km).**

For better illustrative analysis, CSS-1 on Face-4 is presented. The CSS field of view region in the sunlit area of the planet in Fig. 13 is marked with the colored base albedo map. The observed area is getting larger with rising

altitude. However, even the observed area is getting larger, the current readings of each CSS caused by the albedo - without any noise on the sensor- decreases and converges to zero when going up from 500 km to 20,000 km altitude (see Fig. 14) because of the inverse square law of the light intensity.

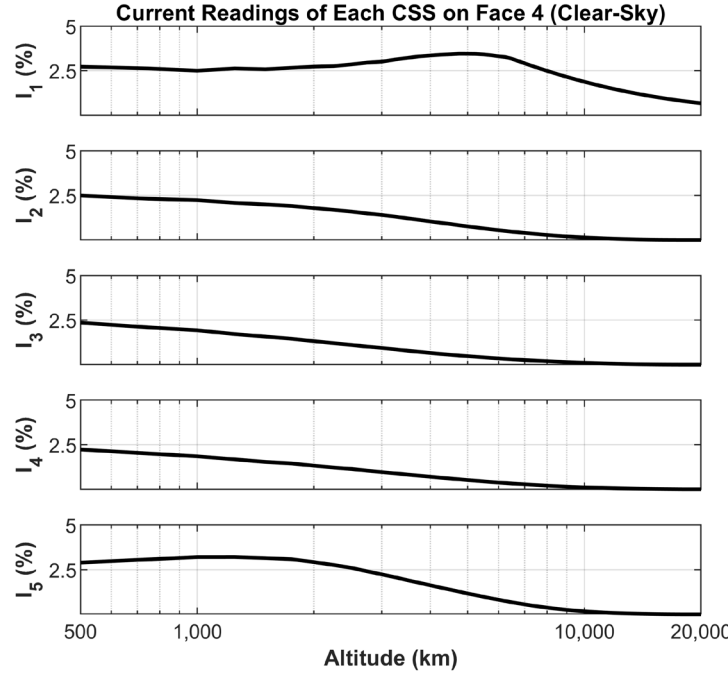


**Fig. 14 Altitude dependent CSS current outputs on Face 4 of the satellite.**

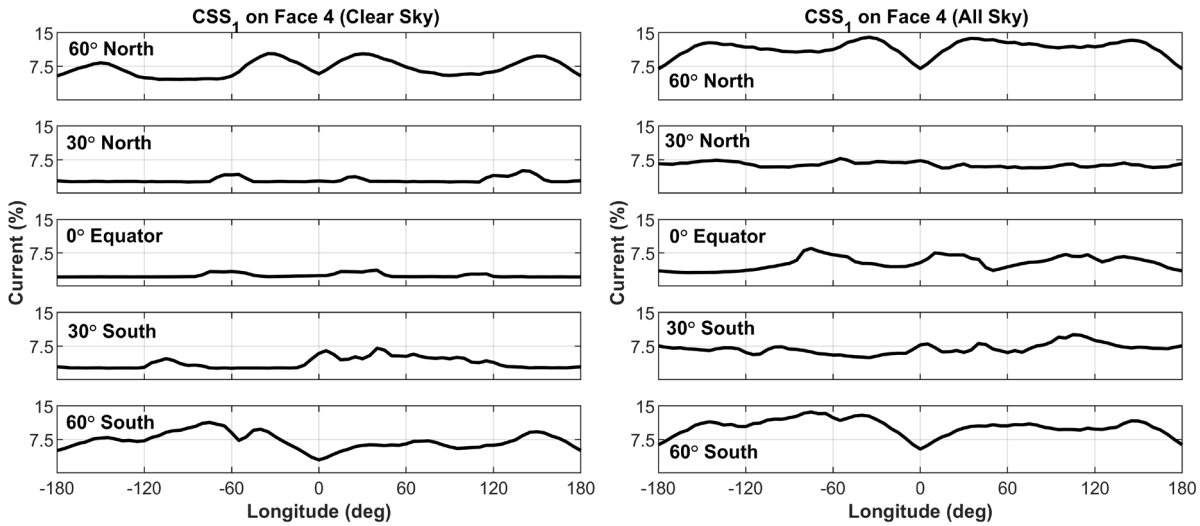


**Fig. 15 Longitude dependent CSS-1 current outputs on Face 4 of the satellite at 800 km under clear-sky (left) and all-sky (right) conditions.**

It is known that there is a large dependency on the latitude, but it is sometimes assumed that only a small dependency on longitude [4, 14, 44]. In order to inspect this assumption, the longitude dependency of the albedo on a

CSS is examined for both cases (clear-sky and all-sky). CSS readings depending on the longitude changes are seen in Fig. 15 for  $\{60^\circ\text{N}, 30^\circ\text{N}, 0^\circ, 30^\circ\text{S}, 60^\circ\text{S}\}$  latitudinal lines. Even it was expected to have similar current readings caused by albedo when differentiating the longitude at high latitudes, outputs on the Panels 1 and 5 of the figures still highly depend on the longitude change of the spacecraft. In fact,  $0^\circ$  latitude differs the least in the clear-sky case. The standard deviations are calculated respectively as  $\sigma_{\text{clear}} = [0.018 \ 0.006 \ 0.004 \ 0.012 \ 0.018]$  for clear-sky condition, and  $\sigma_{\text{all}} = [0.017 \ 0.005 \ 0.014 \ 0.011 \ 0.018]$  for all-sky. However, there is no regular trend seen for differentiating longitudes on the same latitude line; therefore, their effects need to be taken into account. The results from this examination are special to our case but point out that the albedo value at the instrument depends on the longitude. There might be some cases where the albedo is having almost a constant value on a latitude line or a region if several conditions meet simultaneously which is a rare case.

## B. Spacecraft's Attitude Estimation using Earth's Albedo Interfered Sun Sensors

In the second setup, the simulations are performed for a spacecraft with the principal moment of inertia  $I = \text{diag}[0.055 \ 0.055 \ 0.017] \text{ kg m}^2$  on an almost circular near-Earth orbit with 730 km average altitude and with inclination  $i = 96.5^\circ$  starting on 2018 March 1 or 2018 June 1 at 00:00 UTC. The spacecraft is tumbling during the simulations on an orbit propagated by employing the Simplified General Perturbation Version 4 (SGP4) model introduced by Reference [45]<sup>\*</sup>. The sun direction is formulated using the model presented by Vallado [46]. The CSSs are processed at 1 Hz and corrupted by Gaussian zero-mean noise with a standard deviation of 2% (unitless).

The first part of this section is devoted to analyzing the albedo estimation using different albedo models. For this purpose, the models are divided into roughly two different categories as of albedo data based models (empirical albedo models), and the AR albedo model. The estimation procedures for each model category can be seen in Fig. 16 (a) and (b) respectively. The attitude information for the sun direction vector transformation from inertial to body frame is assumed to be estimated by using star trackers with 1 arc second accuracy without considering any misalignments on the sensors. In Fig. 16 (a), the albedo estimation procedure is based on the model requiring to find the sunlit area within the field of view of the sensor and to obtain the albedo coefficient data. Albedo estimation based on the AR model on the other hand does not require any of this information but a two-stage estimation. AR albedo model is also

---

\* The SGP4 source code is available at <http://celestrak.com/publications/AIAA/2006-6753/>.

tested for a one-stage estimation filter but the results were not promising so that only the two-stage estimation filter based on the AR model is proposed to be used for albedo estimation. The estimation procedures utilize the albedo measurements generated by the difference between the CSS's sun direction measurement vector and the modeled sun direction vector transformed into the body frame. However, as the albedo measurements are dependent on the CSS measurements directly, possible sensor-related continuous or time-varying biases will be treated as part of the albedo as well.

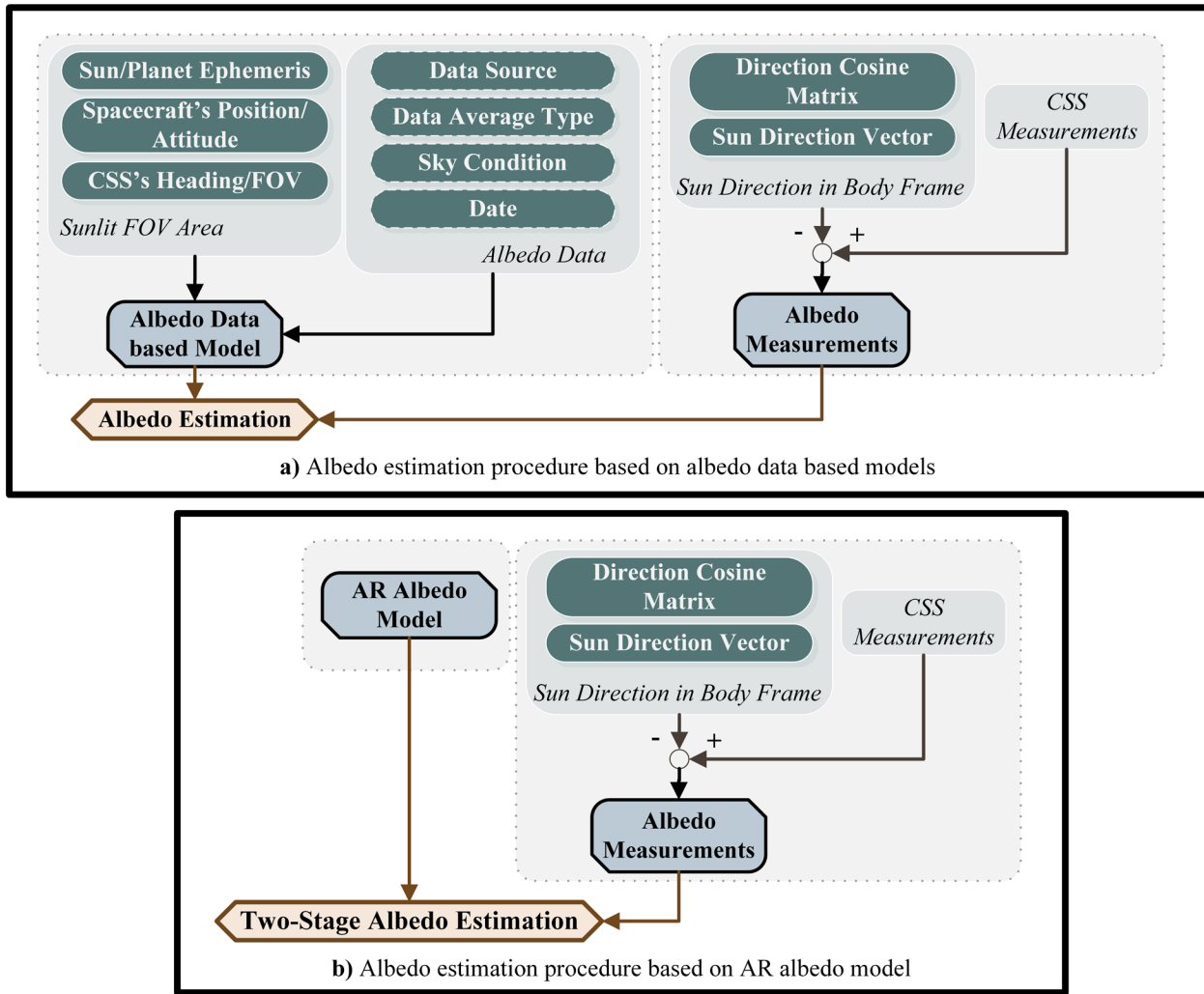


**Fig. 16 Albedo estimation procedure based on albedo data based models (a) and AR albedo model (b).**

The considered albedo models are presented in Table 3. The first two rows list the reference models used in creating the CSS measurements and the rest are selected to see the differences of the model outputs with respect to the references. More than 11 years of CERES albedo coefficient data of Earth is available for the public. So, the first

reference model is based on one month-averaged data over March 2018 for the clear-sky condition while the second reference averaged over the 11 years of data from 2008 to 2018 for July under clear-sky. The first five albedo models are named by sequential numbers and produced using CERES data or a constant value, and the last row shows the AR albedo model. Model 1 uses the albedo data averaged over March 2018 under all-sky. Model 2 uses the albedo data averaged over the whole year of 2018 under clear-sky. Model 3 uses the lookup table presented in Table 1. Model 4 and 5 are based upon the given constant values. Model 3 differs according to which spatial region of the instrument is looking at and in which season the spacecraft is flying. The references are based on two different months in our case, so Model 3 uses two seasons from the lookup table as Season 2 and 3 corresponding to Reference Models 1 and 2 respectively.

**Table 3 Details of the models used for albedo estimation.**

Model Name	Albedo Data	Average Type	Sky Condition	Additional Information
<b>Reference Model 1 (Ref 1)</b>	CERES	Monthly Average March 2018	Clear Sky	-
<b>Reference Model 2 (Ref 2)</b>	CERES	Monthly Average July 2008 - 2018	Clear Sky	-
<b>Model 1</b>	CERES	Monthly Average March 2018	All Sky	-
<b>Model 2</b>	CERES	Yearly Average 2018	Clear Sky	-
<b>Model 3</b>	CERES	Yearly Average 2008-2018	Clear Sky	Lookup table based on spatial and seasonal regions (see Table 1).
<b>Model 4</b>	Constant	-	-	$\alpha = 0.29$
<b>Model 5</b>	Constant	-	-	$\alpha = 0.15$
<b>AR Model</b>	-	-	-	No need to find the sunlit FOV area  Model parameters to be estimated first

The albedo model outputs of Reference Model 1 and 2 are given for three orbits in Fig. 17. There is no albedo contribution during eclipse, as seen from the figure. Therefore, a portion of the simulation is analyzed. First 1000 seconds is selected to be analyzed as the differences between two reference models are more distinct. The albedo model outputs from several albedo models are presented in Fig. 18 for comparing each one of them with Reference

Model 1 on the left panel and Reference Model 2 on the right. As the same condition and configuration for the spacecraft and instrument are used, Models 1 to 5 do not differentiate from one case to another, except Model 3 with different seasonal values. From the results, it can be said that only the AR albedo model follows the reference models for both cases. Among the other albedo models, Model 4, which uses a constant albedo value  $\alpha = 0.29$  over all spatial points on Earth, is superior under Reference Model 1 case, and Model 2 under Reference Model 2 case.

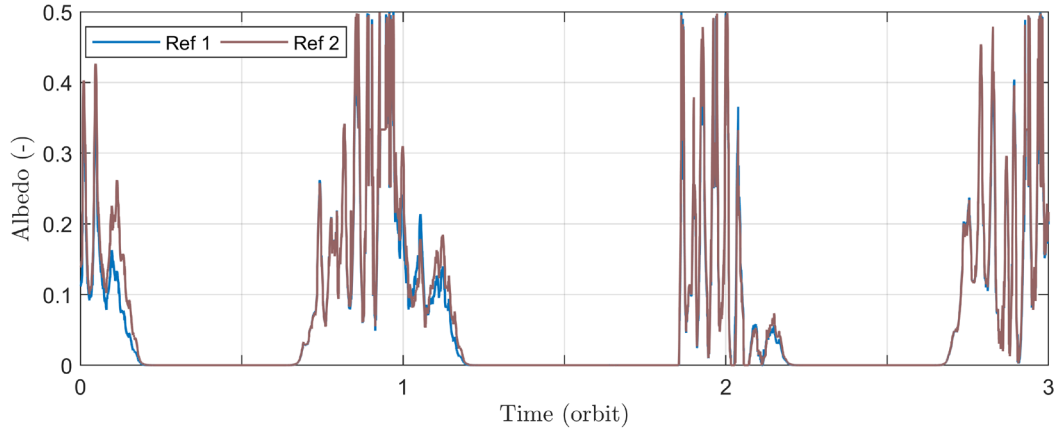


**Fig. 17 Albedo model outputs of Reference Model 1 and 2 for three orbits.**

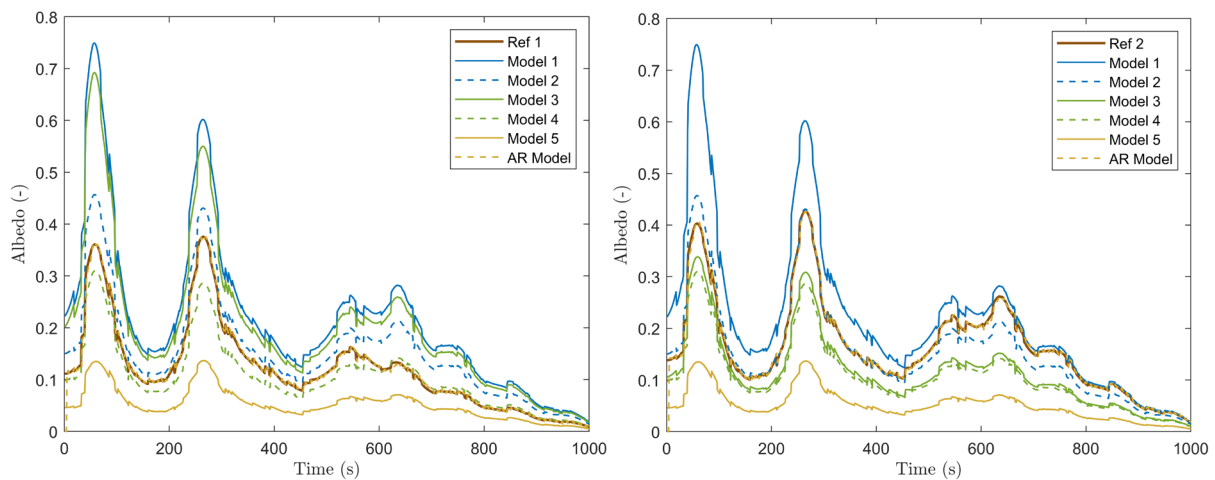


**Fig. 18 Albedo model outputs of several models comparing to Reference Model 1 (left) and Reference Model 2 (right).**

**Table 4 Performance comparison of the albedo models considered.**

Model Name	RMS Error ( - )				Computational Time (s)	
	Model Only		Estimation		Data Processing	Model Processing and Estimation
	Ref 1	Ref 2	Ref 1	Ref 2		
<b>Model 1</b>	0.1201	0.0902	0.0028	0.0027	1.3082	0.0188
<b>Model 2</b>	0.0395	0.0216	0.0028	0.0027	1.4038	0.0188
<b>Model 3</b>	0.0991	0.0612	0.0028	0.0027	0.0014	0.0188
<b>Model 4</b>	0.0277	0.0647	0.0028	0.0027	0.0004	0.0188
<b>Model 5</b>	0.0897	0.1274	0.0028	0.0027	0.0004	0.0188
<b>AR Model</b>	-	-	0.0094	0.0111	-	0.0030

A complementary table is composed of albedo root mean square (RMS) error and the computational time for each model in Table 4. The RMS errors are calculated based on the albedo model outputs and the estimations with respect to the Reference Models. The RMS errors confirm the results of Fig. 18. Albedo data-driven models are also processed under a conventional estimation filter in order to make a fair comparison with the AR albedo model, which is based on a two-stage estimation. The albedo estimations based on Models 1 to 5 give more than three times better accuracy than the AR model-based estimations. However, Models 1 to 5 depend on many parameters, unlike the AR model. In the meantime, the computational burden is lighter when it comes to the AR model as seen from Table 4. AR model does not require any data processing at the beginning, and the total processing and estimation speed is around six times faster than the others.

The limitation of the AR albedo model might be caused by inadequate or faulty albedo measurements as it highly depends on the measurements. For example, if there is a sensor-related bias on CSS in addition to the albedo, this will be compensated by the AR albedo model estimation procedure yet the albedo estimation will not represent the actual albedo this time. This might cause an issue for the other subsystems in need of estimated albedo information such as solar panels. On-ground calibration is suggested for preventing such a problem.

Attitude information is assumed to be known with high accuracy in the first part. As the AR albedo model is greatly dependent on the albedo measurements with a necessity of attitude information, albedo estimations are most likely to be disrupted in the case of no proper attitude information like a malfunction of the star trackers. If there are no star tracker outputs available, magnetometers and/or sun sensors could conceivably be used for attitude

determination purposes. It is possible to use them separately as a single sensor in recursive estimation methods or together for an improved estimation. In the analysis, the estimations are first presented using TAM and CSS pair, then CSS without TAM. Using TAM measurements in the estimations is performed by closing the switches for TAM and Magnetic Field Model boxes seen in Fig. 19 (a) and (b), and open switches are for not using them.

The albedo is assumed to be in the form of Reference Model 2 based on 11-year averaged July CERES albedo data under the clear-sky condition in all cases. A wrong albedo model in the form of Model 4 and AR model that does not require any information other than CSS measurements and attitude of the spacecraft are considered in the attitude and albedo estimation algorithms for comparison. The RG-driven kinematic motion model is used for the attitude estimation filters in this study but the use of a dynamic model with no RGs is also an option [47, 48].

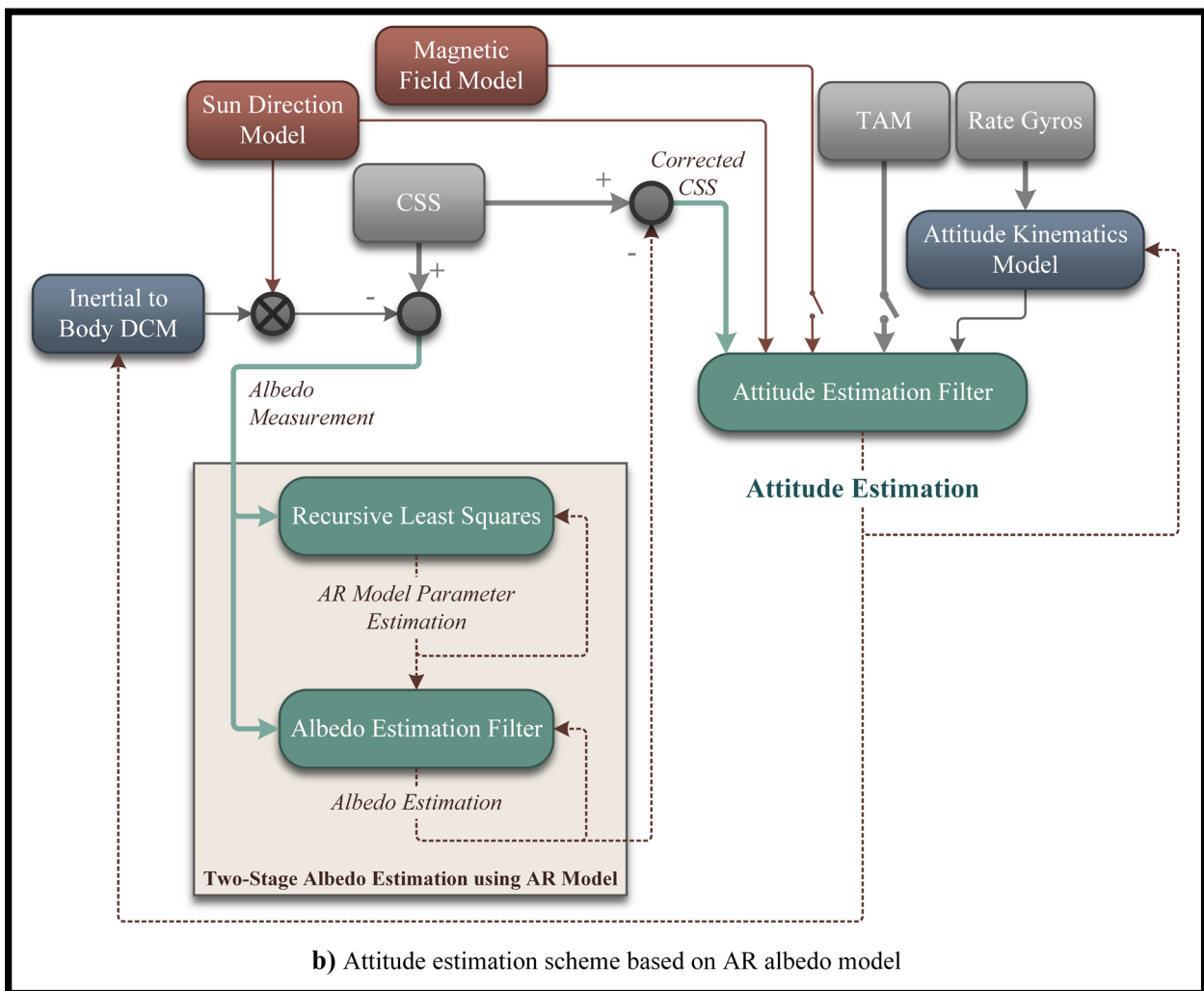
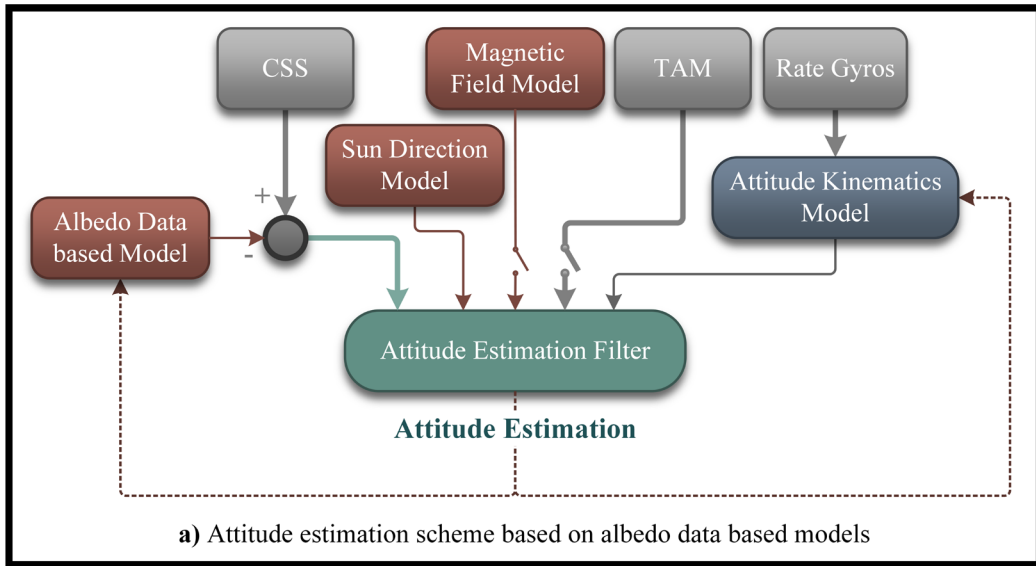


**Fig. 19 Attitude estimation framework based on albedo data based models (a) and AR albedo model (b).**

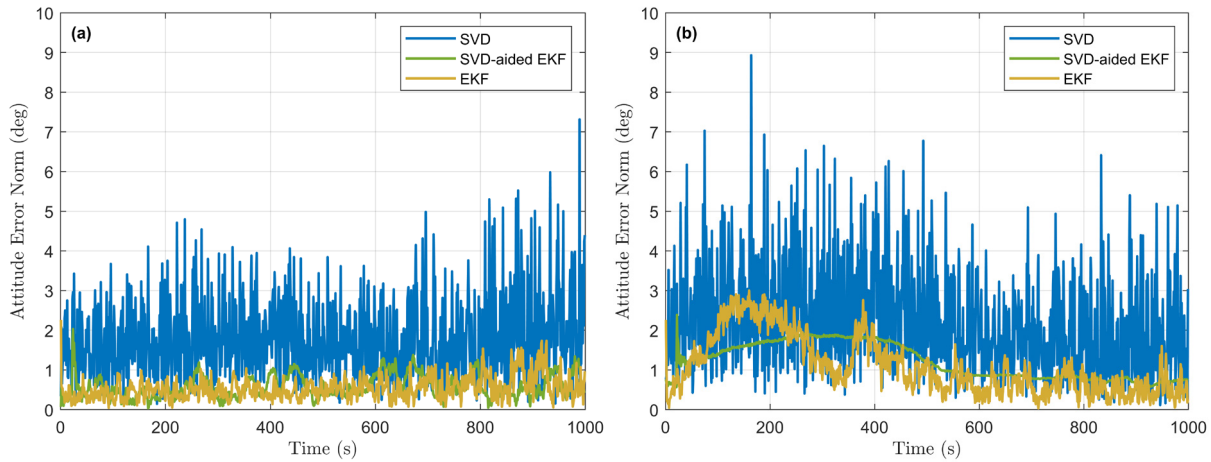


**Fig. 20 Attitude error norms of the SVD, SVD-aided EKF and EKF methods using TAM and CSS with albedo interference based on Model 4 (a) and AR Model (b).**

The “Albedo Data based Model” box in Fig. 19 (a) represents the wrong albedo model (Model 4) in the analysis. The CSS outputs are corrected by using the albedo models before using it in the attitude estimation methods. Attitude is represented by MRPs ( $\sigma_{B/R}$ ) where  $B$  stands for the body and  $R$  for the reference (Earth-centered inertial) coordinates in the simulations but transformed into Euler 3-2-1 angles in degrees for presentation. The estimation error levels of the components vary between different simulations possibly due to the randomized values used in the models and the filters. Therefore, the attitude error norms are presented instead of giving the results in component-by-component. The attitude error norms of the listed estimation methods are given in Fig. 20 (a) using Model 4. The same procedure is applied by replacing the Model 4 with the AR model as presented in Fig. 19 (b). But this time the attitude error is a little more especially in the transient region until compensation at around 600<sup>th</sup> seconds seen in Fig. 20 (b).

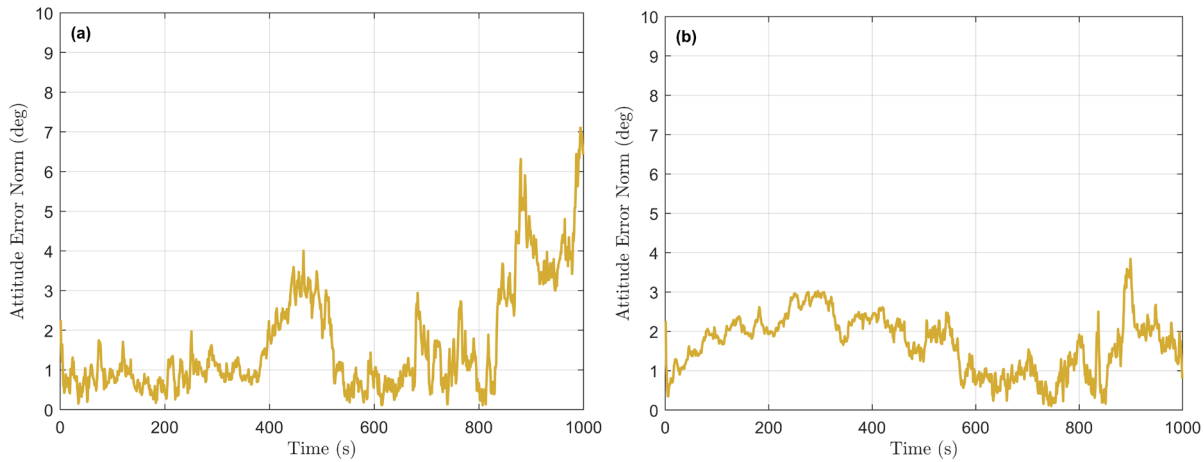


**Fig. 21 Attitude error norms of EKF using CSS with albedo interference based on Model 4 (a) and AR Model (b).**

It is possible to estimate the spacecraft's attitude using only one vector observation in the recursive estimation methods, CSS measurements are used in this case. The structures of Model 4 and AR Model-based estimation filters are shown in Fig. 19 (a) and (b) respectively with open switches for magnetic field related blocks. Having only CSS with albedo interference makes the results deteriorated more as seen in Fig. 21 (a) and (b). The mean attitude estimation errors are given in Table 5.

**Table 5 Attitude angle estimation performance.**

<b>Sensor</b>	<b>Albedo Model</b>	<b>Mean Attitude Error (deg)</b>		
		<b>SVD</b>	<b>SVD-aided EKF</b>	<b>EKF</b>
<b>TAM and CSS</b>	Model 4	1.87	0.58	0.54
	AR Model	2.35	1.45	1.09
<b>CSS</b>	Model 4	-	-	2.45
	AR Model	-	-	1.92

Table 6 is composed using normalized root mean square (NRMS) errors of attitude estimation averaged over 100 Monte Carlo simulations, which confirms the results except that EKF gives slightly improved results than presented in Fig. 20 (b).

**Table 6 Performance comparison of the attitude estimation algorithms considered (Averaged over 100 simulations).**

<b>Sensor</b>	<b>Method</b>	<b>Attitude NRMS Error (%)</b>	
		<b>Model 4</b>	<b>AR Model</b>
<b>TAM and CSS</b>	<b>SVD</b>	1.20	1.82
	<b>SVD-aided EKF</b>	0.53	1.01
	<b>EKF</b>	0.38	0.38
<b>CSS</b>	<b>EKF</b>	2.34	1.70

From the analyses, it is identified that albedo data based models (Models 1-5) differ from the reference models case to case, but on the other hand, the AR albedo model follows the reference. So, it cannot be directly stated which model is the best among the five data-driven albedo models and they can only be evaluated case-by-case. For a fair comparison in the estimation sense, a conventional estimation filter is applied to the albedo models that also follow the reference trend like the AR albedo model. This comparison is made under the assumption of having highly accurate attitude information from star trackers. In terms of computations, AR albedo model processing and estimation speed is around six times faster than the others. Among the albedo data based models, Model 4 ( $\alpha = 0.29$ ) is found to be the best of confirming the first reference, and Model 2 (2018-yearly average) of confirming the second reference. Model 3 using the lookup table formed of seasonal and spatial regions underperformed from the expectations. Based on these, it is recommended to use the AR albedo model because of its consistency between cases. However, AR albedo model is limited with the used albedo measurements which might include CSS related bias. On-ground calibration is suggested for preventing such a problem.

Two sensor configurations and two albedo models (Model 4 and AR Model) are considered in the attitude estimation sense. Overall, EKF is an accurate attitude estimation method with less computational burden than the pre-processed filter (SVD-aided EKF) for TAM – CSS pair. It can be used in CSS-only case as well. The other attitude estimation methods can also be implemented using the proposed framework in Fig. 19. TAM – CSS pair case provides the most accurate attitude estimation when using Model 4 corrections. CSS-only case, on the other hand, provides the most accurate attitude estimation when using AR Model corrections. Therefore, the albedo model to be used can be determined based on the configuration as well.

## VI. Conclusion

This study considers a spacecraft setup close enough to the sun and Earth receiving electromagnetic radiation of direct solar flux and reflected radiation namely albedo in which both are sensed by the sun sensors. Earth's albedo data are obtained from the CERES instrument. By evaluating the data, the maximum albedo of Earth is found in the polar regions and under all-sky conditions. Continental areas have higher albedo values, especially under clear-sky conditions. Albedo contributes to sun sensors from each incremental area of Earth in the sunlit area within the sensor field of view. The albedo intensity has a higher impact on sun sensors when getting closer to Earth.

The main purpose of this study is to find a simple model with less parameter dependency than the empirical albedo models. The second purpose is to estimate the attitude by comprising the corrected CSS measurements free from albedo so as to obtain better accuracy. AR albedo model is proposed, which do not use albedo coefficients depending on the position, time, ground and cloud coverage parameters. To the best of our knowledge, the AR model is used in albedo estimation for the first time in this study. For comparison, five different models are evaluated under the albedo data-driven model in addition to the AR albedo model. The two-stage albedo estimation filter is applied based on the AR model so as to mitigate the albedo error source from the CSS measurements and to feed into the necessary subsystems. It is proposed to use the AR albedo model because of its simplicity and consistency between cases. However, spacecraft's attitude information is necessary to estimate the albedo based on AR model. So, an attitude estimation procedure is also presented using the estimated albedo. The procedure is composed by estimating the albedo first and correcting the CSS after. In this way, it has the advantage that any albedo model is not considered in the last output equations of the attitude estimation filter. The attitude is estimated in accordance with two different sensor configurations by the Kalman-type estimation filters. Three-axis attitude is estimated with around  $4^\circ$  accuracy using only CSS measurements without any correction and around  $2^\circ$  accuracy when CSS is corrected by the AR model.

## Funding Sources

D. Cilden-Guler is supported by ASELSAN (Military Electronic Industries) and TUBITAK (The Scientific and Technological Research Council of Turkey) 2211-C Program for her Ph.D. studies, and partly by Fulbright Visiting Student Researcher Program and TUBITAK 2214-A Program for this research.

## References

- [1] F. L. Markley and J. L. Crassidis, "Sensors and Actuators," in *Fundamentals of Spacecraft Attitude Determination and Control*, New York, NY: Springer New York, 2014, pp. 123–181. ([https://doi.org/10.1007/978-1-4939-0802-8\\_4](https://doi.org/10.1007/978-1-4939-0802-8_4))
- [2] National Aeronautics and Space Administration, "Earth Albedo and Emitted Radiation," Report, Goddard Space Flight Center, Greenbelt, MD, 1971.
- [3] T. W. Flatley and W. A. Moore, "An Earth Albedo Model: A Mathematical Model for the Radiant Energy Input to an Orbiting Spacecraft Due to the Diffuse Reflectance of Solar Radiation From the Earth Below," Technical Memorandum 104596, National Aeronautics and Space Administration, Goddard Space Flight Center, Greenbelt, MD, 1994.
- [4] D. Bhanderi and T. Bak, "Modeling Earth Albedo for Satellites in Earth Orbit," in *AIAA Guidance, Navigation, and Control Conference and Exhibit*, 2005. (<https://doi.org/10.2514/6.2005-6465>)
- [5] G. N. Kuvyrkin and T. M. Menshawy, "Earth's Albedo Input to a Low-Earth-Orbit Satellite based on Local Albedo Coefficients," *J. Spacecr. Rockets*, Vol. 53, No. 4, pp. 792–796, Jul. 2016. (<https://doi.org/10.2514/1.A33349>)
- [6] R. Peyrou-Lauga, "Using Real Earth Albedo and Earth IR Flux for Spacecraft Thermal Analysis," in *47th International Conference on Environmental Systems*, 2017.
- [7] D. Bhanderi, "Modeling Earth Albedo Currents On Sun Sensors for Improved Vector Observation," in *AIAA Guidance, Navigation, and Control Conference and Exhibit*, 2006. (<https://doi.org/10.2514/6.2006-6592>)
- [8] R. V. F. Lopes, A. R. Silva, J. Reloso, G. Absi, and Y. Jun, "Analysis of Albedo Effects on Coarse Sun Direction Determination Algorithms," in *22nd International Symposium on Space Flight Dynamics*, 2011.
- [9] S. A. O'Keefe and H. Schaub, "Sun-direction estimation using a partially underdetermined set of coarse sun sensors," *J. Astronaut. Sci.*, Vol. 61, No. 1, pp. 85–106, 2014. (<https://doi.org/10.1007/s40295-015-0058-9>)
- [10] S. A. O'Keefe and H. Schaub, "Consider-Filter-Based On-Orbit Coarse Sun Sensor Calibration Sensitivity," *J. Guid. Control. Dyn.*, Vol. 40, No. 5, pp. 1300–1303, May 2017. (<https://doi.org/10.2514/1.G001692>)
- [11] S. A. O'Keefe and H. Schaub, "On-Orbit Coarse Sun Sensor Calibration Sensitivity To Sensor And Model Error," in *AAS/AIAA Spaceflight Mechanics Meeting*, 2015, p. AAS 15-392.
- [12] J. C. Springmann and J. W. Cutler, "On-Orbit Calibration of Photodiodes for Attitude Determination," *J. Guid. Control. Dyn.*, Vol. 37, No. 6, pp. 1808–1823, Nov. 2014. (<https://doi.org/10.2514/1.G000175>)
- [13] D. Brasoveanu and J. Sedlak, "Analysis of Earth Albedo Effect on Sun Sensor Measurements based on Theoretical Model and Mission Experience," in *AAS/GSFC 13th International Symposium on Space Flight Dynamics*, 1998, Vol. 1, pp. 435–447.
- [14] P. Appel, "Attitude estimation from magnetometer and earth-albedo-corrected coarse sun sensor measurements," in *Acta Astronautica*, 2005, Vol. 56, No. 1–2, pp. 115–126. (<https://doi.org/10.1016/j.actaastro.2004.09.001>)

- [15] P. Ailliot and V. Monbet, “Markov-switching autoregressive models for wind time series,” *Environ. Model. Softw.*, Vol. 30, pp. 92–101, Apr. 2012. (<https://doi.org/10.1016/j.envsoft.2011.10.011>)
- [16] M. Chandorkar, E. Camporeale, and S. Wing, “Probabilistic forecasting of the disturbance storm time index: An autoregressive Gaussian process approach,” *Sp. Weather*, Vol. 15, No. 8, pp. 1004–1019, Aug. 2017. (<https://doi.org/10.1002/2017SW001627>)
- [17] D. Wang, X. Xu, Y. Yao, Y. Zhu, and J. Tong, “A Hybrid Approach Based on Improved AR Model and MAA for INS/DVL Integrated Navigation Systems,” *IEEE Access*, Vol. 7, pp. 82794–82808, 2019. (<https://doi.org/10.1109/ACCESS.2019.2924593>)
- [18] M. Narasimhappa, “Modeling of Inertial Rate Sensor Errors Using Autoregressive and Moving Average (ARMA) Models,” in *Gyroscopes - Principles and Applications [Working Title]*, IntechOpen, 2019. (<https://doi.org/10.5772/intechopen.86735>)
- [19] S. A. O’Keefe, “Autonomous Sun-Direction Estimation Using Partially Underdetermined Coarse Sun Sensor Configurations,” Aerospace Engineering Sciences Graduate Theses & Dissertations, University of Colorado Boulder, 2015.
- [20] D. V. Titov, M. A. Bullock, D. Crisp, N. O. Renno, F. W. Taylor, and L. V. Zasova, “Radiation in the atmosphere of Venus,” 2007, pp. 121–138. (<https://doi.org/10.1029/176GM08>)
- [21] G. L. Stephens, D. O’Brien, P. J. Webster, P. Pilewski, S. Kato, and J. Li, “The albedo of Earth,” *Rev. Geophys.*, Vol. 53, No. 1, pp. 141–163, Mar. 2015. (<https://doi.org/10.1002/2014RG000449>)
- [22] M. J. Smith, M. F. Goodchild, and P. A. Longley, “Surface and Field Analysis,” in *Geospatial Analysis: A Comprehensive Guide to Principle Techniques and Software Tools*, 6th ed., 2018, pp. 339–425.
- [23] N. G. Loeb *et al.*, “Toward Optimal Closure of the Earth’s Top-of-Atmosphere Radiation Budget,” *J. Clim.*, Vol. 22, No. 3, pp. 748–766, Feb. 2009. (<https://doi.org/10.1175/2008JCLI2637.1>)
- [24] S. Kato, N. G. Loeb, D. A. Rutan, and F. G. Rose, “Clouds and the Earth’s Radiant Energy System (CERES) Data Products for Climate Research,” *J. Meteorol. Soc. Japan*, Vol. 93, No. 6, pp. 597–612, 2015. (<https://doi.org/10.2151/jmsj.2015-048>)
- [25] K. Ito and K. Xiong, “Gaussian filters for nonlinear filtering problems,” *IEEE Trans. Automat. Contr.*, Vol. 45, No. 5, pp. 910–927, May 2000. (<https://doi.org/10.1109/9.855552>)
- [26] E. A. Wan and R. Van Der Merwe, “The unscented Kalman filter for nonlinear estimation,” in *Proceedings of the IEEE 2000 Adaptive Systems for Signal Processing, Communications, and Control Symposium (Cat. No.00EX373)*, 2000, pp. 153–158. (<https://doi.org/10.1109/ASSPCC.2000.882463>)
- [27] S. J. Julier and J. K. Uhlmann, “New extension of the Kalman filter to nonlinear systems,” in *Proc. SPIE 3068, Signal*

*Processing, Sensor Fusion, and Target Recognition VI*, 1997, Vol. 3068. (<https://doi.org/10.1117/12.280797>)

- [28] R. DaForno, F. Reali, S. Bristor, and S. Debei, “Autonomous Navigation of MegSat1: Attitude, Sensor Bias and Scale Factor Estimation by EKF and Magnetometer-Only Measurement,” in *22nd AIAA International Communications Satellite Systems Conference and Exhibit*, 2004. (<https://doi.org/10.2514/6.2004-3183>)
- [29] P. Sekhavat, Q. Gong, and I. M. Ross, “NPSAT 1 Parameter Estimation using Unscented Kalman Filter,” in *Proceedings of the 2007 American Control Conference*, 2007, pp. 4445–4451. (<https://doi.org/10.1109/ACC.2007.4283031>)
- [30] H. Schaub and J. L. Junkins, *Analytical Mechanics of Space Systems*, Second Edition. Reston, VA: American Institute of Aeronautics and Astronautics, 2009. (<https://doi.org/10.2514/4.867231>)
- [31] C. D. Karlgaard and H. Schaub, “Nonsingular attitude filtering using modified rodrigues parameters,” *J. Astronaut. Sci.*, Vol. 57, No. 4, pp. 777–791, 2009. (<https://doi.org/10.1007/BF03321529>)
- [32] C. Hajiyev and M. Bahar, “Attitude Determination and Control System Design of the ITU-UUBF LEO1 Satellite,” *Acta Astronaut.*, Vol. 52, No. 2–6, pp. 493–499, 2003. ([https://doi.org/10.1016/S0094-5765\(02\)00192-3](https://doi.org/10.1016/S0094-5765(02)00192-3))
- [33] K. Vinther, K. F. Jensen, J. A. Larsen, and R. Wisniewski, “Inexpensive Cubesat Attitude Estimation Using Quaternions And Unscented Kalman Filtering,” *Autom. Control Aerosp.*, Vol. 4, No. 1, 2011.
- [34] R. Zanetti, T. Ainscough, J. Christian, and P. D. Spanos, “Q Method Extended Kalman Filter,” *NASA Technical Reports*, 2012. [Online]. Available: <http://ntrs.nasa.gov/archive/nasa/casi.ntrs.nasa.gov/20120017927.pdf>.
- [35] D. Cilden-Guler, M. Raitoharju, R. Piche, and C. Hajiyev, “Nanosatellite attitude estimation using Kalman-type filters with non-Gaussian noise,” *Aerospace Sci. Technol.*, Vol. 92, pp. 66–76, Sep. 2019. (<https://doi.org/10.1016/J.AST.2019.05.055>)
- [36] H. E. Soken, D. Cilden, and C. Hajiyev, “Integration of single-frame and filtering methods for nanosatellite attitude estimation,” in *Multisensor Attitude Estimation: Fundamental Concepts and Applications*, H. Fourati and D. E. C. Belkhiat, Eds. CRC Press, 2016, pp. 463–484. (<https://doi.org/10.1201/9781315368795>)
- [37] G. Wahba, “Problem 65-1: A Least Squares Estimate of Satellite Attitude,” *Soc. Ind. Appl. Math. Rev.*, Vol. 7, No. 3, p. 409, 1965.
- [38] D. Cilden-Guler, E. S. Conguroglu, and C. Hajiyev, “Single-Frame Attitude Determination Methods for Nanosatellites,” *Metrol. Meas. Syst.*, Vol. 24, No. 2, pp. 313–324, 2017.
- [39] F. L. Markley and D. Mortari, “Quaternion Attitude Estimation using Vector Observations,” *J. Astronaut. Sci.*, Vol. 48, No. 2, pp. 359–380, 2000.
- [40] E. Thébault *et al.*, “International Geomagnetic Reference Field: the 12th generation,” *Earth, Planets Sp.*, Vol. 67:69, 2015. (<https://doi.org/10.1186/s40623-015-0228-9>)
- [41] F. Markley and J. Crassidis, “Environment Models,” in *Fundamentals of Spacecraft Attitude Determination and Control*,

New York, NY: Springer New York, 2014, pp. 403–425. ([https://doi.org/10.1007/978-1-4939-0802-8\\_11](https://doi.org/10.1007/978-1-4939-0802-8_11))

- [42] L. Chen *et al.*, “Earth polar motion parameters high accuracy differential prediction,” in *Lecture Notes in Electrical Engineering*, 2014, Vol. 323, pp. 71–79. ([https://doi.org/10.1007/978-3-662-44687-4\\_7](https://doi.org/10.1007/978-3-662-44687-4_7))
- [43] J. P. Snyder and P. M. Voxland, “An album of map projections,” 1989. (<https://doi.org/10.3133/pp1453>)
- [44] N. S. Khalifa and T. E. Sharaf-Eldin, “Earth albedo perturbations on low earth orbit cubesats,” *Int. J. Aeronaut. Sp. Sci.*, Vol. 14, No. 2, pp. 193–199, 2013. (<https://doi.org/10.5139/IJASS.2013.14.2.193>)
- [45] D. A. Vallado and P. Crawford, “SGP4 orbit determination,” in *AIAA/AAS Astrodynamics Specialist Conf.*, 2008. (<https://doi.org/10.2514/6.2008-6770>)
- [46] D. A. Vallado, *Fundamentals of Astrodynamics and Applications (3rd Ed.)*, Vol. 21. USA: Microcosm Press/Springer, 2007.
- [47] R. Burton, S. Rock, J. Springmann, and J. Cutler, “Online attitude determination of a passively magnetically stabilized spacecraft,” *Acta Astronaut.*, Vol. 133, pp. 269–281, Apr. 2017. (<https://doi.org/10.1016/j.actaastro.2017.01.024>)
- [48] C. Hajiyev, D. Cilden, and Y. Somov, “Gyro-free attitude and rate estimation for a small satellite using SVD and EKF,” *Aerospace Sci. Technol.*, Vol. 55, pp. 324–331, 2016. (<https://doi.org/10.1016/j.ast.2016.06.004>)